Monthly Notices of the ROYAL ASTRONOMICAL SOCIETY

MNRAS **524,** 6024–6051 (2023)
Advance Access publication 2023 July 24

https://doi.org/10.1093/mnras/stad2192

Relativistic coronal mass ejections from magnetars

Praveen Sharma [1]★ Maxim V. Barkov [2] and Maxim Lyutikov [1]

[1] *Department of Physics, Purdue University, 525 Northwestern Avenue, West Lafayette, IN 47907, USA*
[2] *Institute of Astronomy, Russian Academy of Sciences, Moscow 119017, Russian Federation*

Accepted 2023 June 30. Received 2023 June 12; in original form 2023 February 27

ABSTRACT

We study dynamics of relativistic coronal mass ejections (CMEs), from launching by shearing of foot-points (either slowly – the 'Solar flare' paradigm, or suddenly – the 'star quake' paradigm), to propagation in the preceding magnetar wind. For slow shear, most of the energy injected into the CME is first spent on the work done on breaking through the overlaying magnetic field. At later stages, sufficiently powerful CMEs may lead to the 'detonation' of a CME and opening of the magnetosphere beyond some equipartition radius $r_{\rm eq}$, where the decreasing energy of the CME becomes larger than the decreasing external magnetospheric energy. Post-CME magnetosphere relaxes via the formation of a plasmoid-mediated current sheet, initially at $\sim r_{\rm eq}$, and slowly reaching the light cylinder. Both the location of the foot-point shear and the global magnetospheric configuration affect the frequent/weak versus rare/powerful CME dichotomy – to produce powerful flares, the slow shear should be limited to field lines that close in near the star. After the creation of a topologically disconnected flux tube, the tube quickly (at $\sim$ the light cylinder) comes into force-balance with the preceding wind and is passively advected/frozen in the wind afterward. For fast shear (a local rotational glitch), the resulting large amplitude Alfvén waves lead to the opening of the magnetosphere (which later recovers similarly to the slow shear case). At distances much larger than the light cylinder, the resulting shear Alfvén waves propagate through the wind non-dissipatively.

Key words: MHD – Sun: coronal mass ejections (CMEs) – stars: magnetars – stars: magnetic field – stars: neutron – (transients:) fast radio bursts.

1 INTRODUCTION

Magnetars, a class of highly magnetized neutron stars, produce X-ray and γ-ray bursts (Usov 1992; Thompson & Duncan 1995; Komissarov & Barkov 2007; Mereghetti 2008; Kaspi & Beloborodov 2017), and occasional giant flares (Hurley et al. 2005; Palmer et al. 2005). Discoveries related to fast radio bursts (Cordes & Chatterjee 2019; Petroff, Hessels & Lorimer 2019), especially simultaneous observations of radio and X-ray bursts from a magnetar (Bochenek et al. 2020; CHIME/FRB Collaboration 2020; Mereghetti et al. 2020; Ridnaia et al. 2021) renewed interest in the dynamics of magnetar's explosions.

To set up the stage, we first qualitatively divide FBR models into two types – magnetospheric and wind models. Also qualitatively, we divide magnetar flares' models into *Solar flare paradigm* and *Starquake paradigm*, with a clear understanding that the actual separation of models is/may not be as clearly defined.

In the case of FRBs, one set of theories advocates that FRBs are magnetospheric events (e.g. Lyutikov 2003; Popov & Postnov 2013; Lyutikov, Burzawa & Popov 2016; Lyutikov & Popov 2020). An alternative suggestion is the generation of FRBs in the wind or in the wind termination shock (e.g. Lyubarsky 2014; Beloborodov 2017; Metzger, Margalit & Sironi 2019; Barkov & Popov 2022; Khangulyan, Barkov & Popov 2022; Thompson 2023). Observations of contemporaneous magnetar X-ray flares and FRB strengthened the evidence for magnetospheric *loci* (as argued by Lyutikov & Popov 2020); the detection of sub-second periodicity (CHIME/FRB Collaboration 2022) leaves little doubt in our view. The recent detection of antiglitch in FRB-associated magnetar Younes et al. (2023) is also consistent with the magnetospheric model, see Lyutikov (2013).

The wind models of FRBs appeal to the generation of a strong shock or magnetic shell that propagates through the wind. As we demonstrate in this paper, the assumption of strong shock/magnetic shell propagating *through* the wind is incorrect: the magnetic shells can naturally come into force balance near the light cylinder, and are then passively advected with the wind. We model quite a small magnetosphere radius $R_{\rm LC} = 5R_{\rm NS}$. It allows keeping pressure balance due to small Lorentz factors of the flow. In the case of a larger dynamical range (10^4) it can be not so. Acceleration of the blob inside the magnetosphere up to $\Gamma > 10$ will lead to loss of the casual connection and the blob can escape in strongly unbalanced conditions and form an explosion-like solution in the wind zone.

As for magnetars' flares, the *Solar flare paradigm* for magnetar explosions (Lyutikov 2006, 2015) argues that the underlying mechanism that causes magnetars' flares may be similar to those operating in the solar corona. According to the model, GFs are magnetospheric events. An alternative view is that magnetar flares are crustal events (Thompson & Duncan 1995). In the *Solar flare paradigm*, the energy that will eventually power magnetar flares is first stored inside the neutron star right following the core-collapse of the progenitor star. Slowly over time, hundreds to thousands of years, the internal magnetic twist is pushed into the magnetosphere via Hall (electron-MHD) drift (Goldreich & Reisenegger 1992; Gourgouliatos et al.

★ E-mail: sharm303@purdue.edu

2013; Wood, Hollerbach & Lyutikov 2014), gated by slow, plastic deformations of the neutron star crust (Lyutikov 2015). This leads to the gradual twisting of the external magnetospheric field lines, on time-scales much longer than the magnetar's GF, and creates active magnetospheric regions similar to the Sun's spots. As more and more current is pushed into the magnetosphere, it eventually reaches a point of dynamical instability. The loss of stability leads to a rapid restructuring of magnetic configuration, on the Alfven crossing time-scale, to the formation of narrow current sheets, and the onset of magnetic dissipation. As a result, a large amount of magnetic energy is converted into the kinetic energy of bulk motion and radiation (Lyutikov 2003; Komissarov, Barkov & Lyutikov 2007; Ripperda et al. 2019; Yuan et al. 2020). The coherent emission may be produced due to some kind of plasma instability, for example, via the free electron laser mechanism (Lyutikov 2021). Perhaps the best argument in favour of the 'Solar flare paradigm' is that the observed sharp rise of γ-ray flux during GF, on a time-scale similar to the Alfvén crossing time of the inner magnetosphere, which takes $\sim$0.25 msec (Palmer et al. 2005). This unambiguously points to the magnetospheric origin of GFs (Lyutikov 2006). Since in the *Solar flare paradigm*, GFs are magnetospheric events, no large baryonic loading is expected in the ensuing outflows.

Another model of magnetars' flares, which we call the *Starquake model* of Thompson & Duncan (1995, 2001) (though the 'starquake' is not used in these papers – we thank Chis Thompson for pointing this out – we use this term as a classification marker; the models do appeal to crustal faults), whereas the sudden fracture of the crust leads to the fast motion of the magnetic foot-points. (Levin & Lyutikov 2012, criticized this set-up: even if the elastic properties of the crust allow the creation of a shear crack, the strongly sheared magnetic field around the crack leads to a back-reaction from the Lorentz force which does not allow large relative displacement of the crack surfaces.)

For the present purposes, the difference between the slow shear of the *Solar flare* and the fast shear of the *Starquake* models is that for the slow shear the whole magnetosphere remains in the causal contact, while the fast shear corresponds to a packet of Alfvén waves generated by the foot-point motions. We emphasize that our separation of models into *Solar flare – Starquake* clearly misses many details and is introduced here to highlight the two different dynamics regimes in the ensuing discussion.

In this paper, we seek answers to the two sets of questions, one related to launching the CMEs from the magnetosphere, and the second related to the propagation of the resulting structures through the wind: (i) how the model of sheared/inflated magnetic flux tubes in the Sun (Antiochos, DeVore & Klimchuk 1999) transports into relativistic highly magnetized regime; (ii) what is the role of the light cylinder in generating the CMEs; (iii) what underlying physical parameters distinguish magnetars' giant flares, from the less energetic bursts; (iv) what is the dynamics of magnetospheric perturbation as they enter the wind. By the FRB-magnetar association, these questions may carry the answer to why FRBs are different. Investigations are done with the code PHAEDRA (Parfrey, Beloborodov & Hui 2012), Appendix 3.1. The code invokes force-free electrodynamics, an appropriate limit for the study of neutron star magnetosphere, considering their extremely high magnetic field. In this limit, hydrodynamic forces can be safely neglected and therefore the electromagnetic Lorentz force can be approximated as zero.

The plan of the paper is as follows. In Section 2, we describe theoretical expectations that would guide us through the following research. In Section 3, we describe the code. In Section 4, we concentrate on the innermost dynamics of the CMEs, neglecting rotation/presence of the light cylinder. In Section 5 (slow shear), we adopt a model of generation of Solar CMEs by Antiochos et al. (1999), Antiochos et al. (2007) to relativistic *rotating* magnetospheres of neutron stars. In Section 6 (fast shear), we consider dynamics of a 'glitched magnetosphere' – when a part of the neutron star's crust experience a sudden change in the rotational angular velocity. In Section 7, we consider dynamics, from the magnetospheres to the wind, of an ejected magnetic flux tube.

2 MAGNETAR'S CMES

2.1 The *Solar Flare* paradigm

Coronal mass ejections (CMEs) are the most explosive events in our Solar system and have been long studied in solar physics (Forbes 2000; Vourlidas et al. 2002). According to the model of Solar flares by Antiochos et al. (1999), Antiochos et al. (2007), the underlying cause of the manifestations of solar activity – CMEs, eruptive flares, and filament ejections – is the disruption of a force balance between the upward pressure of the strongly sheared field of a filament channel and the downward tension of a potential (non-current carrying) overlying field. Thus, an eruption is driven solely by the magnetic free energy stored in a closed, sheared magnetic field that opens toward infinity during a CME. Initially, the magnetic field has a complicated multipolar topology while reconnection between a sheared arcade and neighboring flux systems triggers the eruption. We also mention an important Aly's theorem, that open topologies have the largest energy given poloidal magnetic field distribution on the surface (Aly 1991). The presence of the light cylinder changes this picture: if an arc reaches the light cylinder it will become open.

We first explore models of magnetar giant flares based on the same paradigm as Solar Flares and CME (Antiochos et al. 1999, 2007), that they are driven by slow surface shear leading to catastrophic rearrangement of the neutron star's magnetospheric fields.

The principal difference between solar and magnetar CMEs is that the magnetar plasma is relativistic and strongly magnetized, with Alfven velocity of the order of the speed of light. Perhaps it is more correct to them coronal flux ejections (Jens Mahlmann, private communication), but we keep the more familiar notation of a CME. In addition, the presence of a light cylinder plays the most important part in the generation of CMEs in magnetars, if compared with non-rotating calculations of Antiochos et al. (1999, 2007), the light cylinder is the analogue of the Alfven surface in rotating stars.

Through numerical experiments, we found that several complementary ingredient control the overall dynamics of the generation of CMEs in magnetars: global magnetospheric structure, rotation, and the location of shear foot points. To make the following discussion clear, the term 'shearing' refers to the dynamical motion of magnetic foot-points.

We first study step-by-step different global configurations and different shearing prescriptions. In Appendix 3.1, we study separately/reproduce analytical results for separate 'ingredients' of the model: (ii) Sheared non-rotating magnetospheres, Appendix 4.1; (ii) Rotating stars with no foot-point shearing, Appendix B and in particular Michel's solution, Fig. B1.

2.2 Theoretical expectations

2.2.1 The set-up

Let us first discuss the dynamics of topologically isolated flux tubes/magnetic blobs (called CME below) injected deep within

Table 1. Typical scales for dynamics of CME injected within the magnetosphere. Only a small fraction of the injected energy remains within the CME after it escapes from the magnetosphere.

Model	Flux tube	Small CME	Large CME ($R_{\rm CME,\,0} \sim R_{\rm NS}$)
The initial volume of CME	$2\pi R_{\rm NS} \times \pi R^2_{\rm CME,0}$, flux tube	$(4\pi/3) R^3_{\rm CME,0}$, sphere	$(4\pi/3) R^3_{\rm CME,0}$, sphere
Injected energy $E_{\rm CME,\,0}$	$2\pi R_{\rm NS} R^2_{\rm CME,0} B_0^2/(8\pi)$	$(4\pi/3) R^3_{\rm CME,0} B_0^2/(8\pi)$	$(4\pi/3) R^3_{\rm CME,0} B_0^2/(8\pi)$
CME's linear size at r $R_{\rm CME}/R_{\rm CME,\,0}$	$\left(\frac{r}{R_{\rm NS}}\right)^{3/2}$	$\left(\frac{r}{R_{\rm NS}}\right)^{3/2}$	$\left(\frac{r}{R_{\rm NS}}\right)^{3}$
Energy $E_{\rm CME}/E_{\rm CME,\,0}$ at r	$(R_{\rm NS}/r)^2$	$(R_{\rm NS}/r)^{3/2}$	$(R_{\rm NS}/r)$
Equipartition radius $r_{\rm eq}/R_{\rm NS}$	$\eta_{\rm CME}^{-1}$	$\eta_{\rm CME}^{-2/3}$	$\eta_{\rm CME}^{-2/3}$
Energy remaining at $r_{\rm eq}$	$\eta_{\rm CME}^{2}$	$\eta_{\rm CME}$	$\eta_{\rm CME}$

a magnetosphere so that the presence of a light cylinder is not important. (By topologically isolated structured, we mean that no magnetic field line penetrates the boundary.) Consider an injected isolated magnetic structure – two possible geometries include a magnetic flux tube and magnetic ball. Let the injection occur near the stellar surface with

Typical size $R_{\rm CME,\,0} \leq R_{\rm NS}$ and associated energy $E_{\rm CME,\,0}$, Table 1. The magnetic field inside the CME is of the order of the surface magnetic field B_0 so that initially the CME is just slightly unbalanced – the internal magnetic field matches approximately the magnetospheric field. The gradient of the external field pushes the CME out.

An important parameter is the total magnetic energy of the magnetosphere,

$$E_{\rm B,NS} \sim B_0^2 R_{\rm NS}^3. \tag{1}$$

Naturally, the injected energy is much smaller than the total energy,

$$\eta_{\rm CME} = \frac{E_{\rm CME,0}}{E_{\rm B,NS}}. \tag{2}$$

Conservation of the magnetic flux within CME plays the most important role. The injected flux is

$$\Phi_B \sim B_0 R^2_{\rm CME,0} = {\rm Const} = B_{\rm CME} R^2_{\rm CME}. \tag{3}$$

It is conserved during evolution. Thus, magnetic field inside is

$$B_{\rm CME} = B_0 \left(\frac{R_{\rm CME,0}}{R_{\rm CME}}\right)^2. \tag{4}$$

We can then identify three different geometrical cases: (i) flux tube (a toroidally symmetric configuration), (ii) small magnetic ball (spherical ball displaced from the centre); (iii) large magnetic ball ($R_{\rm CME,\,0} \sim R_{\rm NS}$) (centred ball). In the 'large magnetic ball' case, the quasi-spherical injected structure is of the order of the neutron star from the beginning.

Importantly, we can then identify three regimes for the dynamics of the CME: (i) 'breaking-out'; (ii) 'detonation'; (iii) magnetospheric recovery and CME's expansion in the wind, Fig. 1. During the early 'breaking-out' phase, the CME expands while doing work on the overlaying magnetic field. As a result, the energy of the CME reduces dramatically, Table 1. During the 'detonation' stage, the CME expands nearly freely, opening the magnetosphere after the CME's break-out, the magnetosphere recovers by forming a current sheet, while the CME is mostly passively advected with the wind.

2.2.2 *The 'breaking-out' stage*

At the 'breaking-out' stage, the internal magnetic field (4) matches the magnetospheric field at the location of the CME,

$$B_{\rm CME} = B_{\rm NS}(r) = B_0 \left(\frac{r}{R_{\rm NS}}\right)^{-3} \tag{5}$$

(assuming $R_{\rm CME} \ll r$; this is not applicable for the 'large CME' case, right-hand column in Table 1). Combining (4) and (5),

$$\frac{R_{\rm CME}}{R_{\rm CME,0}} = \left(\frac{r}{R_{\rm NS}}\right)^{3/2}. \tag{6}$$

Thus, the cross-sectional area $\propto R^2_{\rm CME} \propto r^3$. This scaling is true for both the flux tube case and the small blob case. Importantly, the CME expands laterally

$$\Delta\theta = \frac{R_{\rm CME}}{r} = \frac{R_{\rm CME,0}}{R_{\rm NS}} \left(\frac{r}{R_{\rm NS}}\right)^{1/2}. \tag{7}$$

As the CME is breaking-out through the overlaying magnetic field, it does work on the magnetospheric magnetic field. As a result, its internal energy sharply decreases: *at least*, as the ratio of the CME energy to the total energy of the magnetosphere, η_E, Table 1:

$$\frac{r_{\rm eq}}{R_{\rm NS}} \sim \begin{cases} \frac{E_{\rm B,NS}}{E_{\rm CME,0}} = \eta_{\rm CME}^{-1}, & \text{spherical CME} \\ \left(\frac{E_{B,NS}}{E_{\rm CME,0}}\right)^2 = \eta_{\rm CME}^{-2}, & \text{flux tube} \end{cases}. \tag{8}$$

We arrive at an important conclusion: only a small fraction of the injected CME's energy affects the wind, at $r \geq R_{\rm LC}$ – most energy is spent on work against the overlaying magnetic field. Later on, when the magnetosphere recovers, the energy deposited into the magnetosphere during CME break-out is dissipated in the newly created current sheet, see Fig. 8, on time-scales much longer than the dynamic time's scale of the injection.

2.2.3 *The 'detonation' stage*

The dynamics change from 'breaking-out' to 'detonation' when the total energy contained in the confining magnetic field exterior to the position of the CME ($\sim B_0^2 R_{\rm NS}^6 r^{-3}$) becomes smaller than the CME's internal energy (equivalently, when the size of the CME becomes comparable to the distance to the star). This occurs at some equipartition radius $r_{\rm eq}$, possibly within the light cylinder, see Table 1 and equation (8).

Beyond the $r_{\rm eq}$ the dynamics change: The CME has much more energy than the confining dipolar magnetic field (from $r_{\rm eq}$ to infinity) – as a result, the expansion enters 'detonation stage' – nearly vacuum-like expansion (Barkov et al. 2022). At this stage, most of the magnetic field is concentrated near the surface of exploding

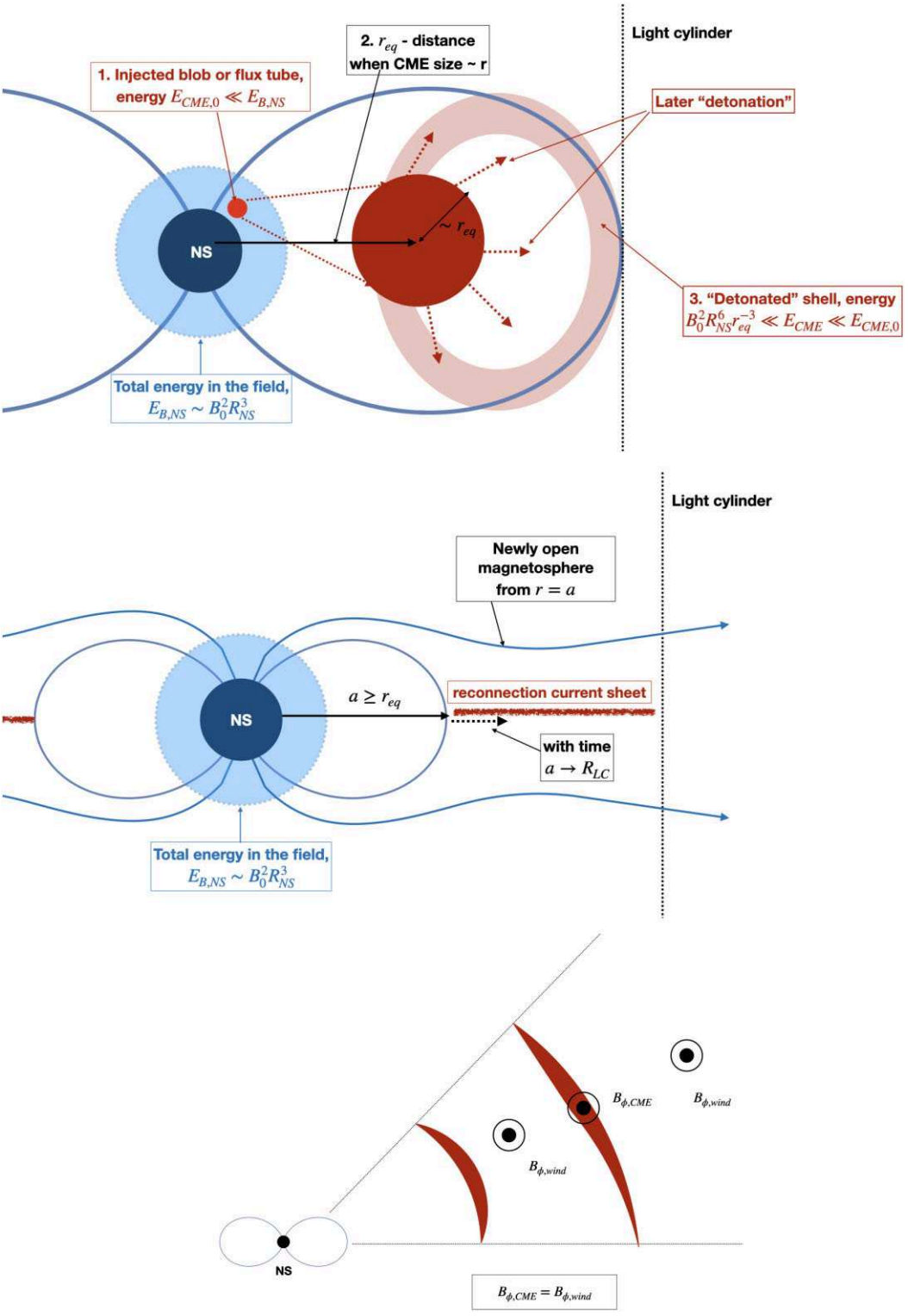

Figure 1. CME dynamics inside the magnetosphere and in the wind. Top panel: A CME, a flux tube or magnetic blob, carrying initial energy $E_{\rm CME,\,0}$ is released near the surface. The energy of the CME is much smaller than the total magnetic energy of the magnetosphere, $E_{\rm CME,\,0} \ll E_{\rm B,\,NS}$. As the CME expands, it is doing work on the overlaying magnetic field, and loses energy. Sufficiently powerful CME may still reach a size comparable to the local distance to the star $r_{\rm eq}$ (while still within the light cylinder). After that, the injected structure would expand quasi-spherically, opening field lines beyond $r_{\rm eq}$. Central panel: post-explosion relaxation. Generation of CME leads to the opening of the magnetosphere at $r_{\rm eq} \leq R_{\rm LC}$. The post-CME magnetosphere recovers by forming a current sheet from $r_{\rm eq}$ to $R_{\rm LC}$. Bottom panel: CME in the wind. A flux tube is injected within the magnetosphere, CME first expands with the magnetosphere, losing energy doing work on the magnetospheric fields to break out, coming to a force balance near the light cylinder, and then is advected passively within the wind as a shell of constant radial and lateral extension.

structure. Most importantly, the whole structure becomes causally disconnected, in a sense that various parts of the expanding blob lose causal contact with each other.

To enter the 'detonation' stage, the radius $r_{\rm eq}$ should be (much) smaller than the light cylinder radius. This requires sufficiently high injection energy, for example, for 'small CMR' column in Table 1,

$$\frac{E_{\rm CME,0}}{E_{B,NS}} \gg \frac{R_{\rm NS}}{R_{\rm LC}} = 2\times 10^{-4}\, P^{-1}, \tag{9}$$

where P is the spin period in seconds. Thus, for a spin period of 1 s, only CMEs that carry energy much larger few thousandths of the total magnetospheric energy reach the 'detonation' stage.

For example, for a magnetar with surface field $B_{\rm NS} = 10^{15}$, the total magnetospheric energy $E_{\rm B,NS} \sim 10^{48}$ erg. Then to enter the detonation stage, the CME should have energy $\geq 10^{44} P^{-1}$ erg. Only very powerful events experience the detonation stage. Even if the CME's energy exceeds the critical, only a small fraction, at most $\sim\eta_{\rm E}$ is transferred to the wind in the form of an EM pulse.

For very energetic explosions, when the equipartition radius $r_{\rm eq}$ is smaller than the light cylinder, the resulting CME 'detonates': creating a causally disconnected shell of thickness $\sim r_{\rm eq}$ that expands freely within the magnetosphere. Locally, the dynamics are governed by the solutions of Lyutikov (2010) and Lyutikov & Hadden (2012) describing the 1D expansion of magnetized fluid into the vacuum. Most of the magnetic energy is concentrated near the surface of the expanding ball (see also Fig. 6).

2.2.4 *Magnetospheric recovery*

The 'detonation' stage, if it occurs, leads to a temporary opening of the magnetosphere beyond the radius $r_{\rm eq}$. The post-CME magnetosphere recovers by forming a current sheet from $r_{\rm eq}$ to $R_{\rm LC}$, Fig. 1 middle panel. Recovery proceeds slowly – the rate of recovery is controlled by dissipative processes in the current sheet.

For $r_{\rm eq} \ll R_{\rm LC}$ the overall magnetic structure can be approximated as a magnetosphere plus diamagnetic disc (Aly 1980; Lyutikov 2023). In this configuration, the structure of the magnetosphere beyond $r_{\rm eq}$ is approximately monopolar (the case of a balanced magnetic dipole in the notation of Lyutikov 2023). The location of the inner edge of the reconnection current sheet a slowly approaches the light cylinder. At each moment, the spin-down power

$$\begin{aligned} L_{\rm sd} &\approx B_{\rm NS}^2 \frac{R_{\rm NS}^6 \Omega^2}{c a^2} \approx \left(\frac{R_{\rm LC}}{a}\right)^2 \times L_{\rm sd,dipole} \gg L_{\rm sd,dipole}, \\ L_{\rm sd,dipole} &\approx B_{\rm NS}^2 \frac{R_{\rm NS}^6 \Omega^4}{c^3}. \end{aligned} \tag{10}$$

2.2.5 *Beyond light cylinder*

Dynamics beyond the light cylinder depend on whether the CME reached the detonation stage or not. In the more likely scenario, when the detonation stage is not reached, the CME is just frozen into the wind, with the lateral and radial extensions remaining nearly constant, see Fig. 1, bottom panel, so that its cross-section S and internal magnetic field evolve according to

$$\begin{aligned} &B_0 S \sim \Delta r \times r \Delta\theta \propto r, \\ &B_{in} = \Phi_0 / S \propto r^{-1}. \end{aligned} \tag{11}$$

(Φ_0 is the value of the injected flux.) The scaling of $B_{\rm in}$ (11) matches the scaling of the external wind magnetic field. *Thus, after reaching a force balance close to the light cylinderthe ejected flux tube remains in force balance with the wind and is passively advected.* The flux tube expands along a conical trajectory, with constant radial thickness. The energy contained in the flux tube remains constant: The expanding magnetic flux tube does not do any work on the surrounding wind.

If the flare energy is sufficiently large and the detonation stage is achieved, the magnetosphere will open up at $r_{\rm eq}$. As a result, an electromagnetic pulse will be launched in the wind. The energy of the pulse will be much smaller than the initial injection energy, $E_{\rm CME}(r_{\rm eq}) \ll E_{\rm CME,0}$.

3 SIMULATIONS WITH PHAEDRA CODE

3.1 Numerical method

In this paper, we study the dynamics of sheared magnetospheres using time-dependent numerical simulations with the pseudo-spectral simulation code PHAEDRA (Parfrey et al. 2012). The code solves Maxwell's equations in spherical, axisymmetric geometry.

$$\begin{aligned} \frac{1}{c}\frac{\partial \boldsymbol{B}}{\partial t} &= -\nabla \times \boldsymbol{E}, \\ \frac{1}{c}\frac{\partial \boldsymbol{E}}{\partial t} &= \nabla \times \boldsymbol{B} - \frac{4\pi}{c}\boldsymbol{J}. \end{aligned} \tag{12}$$

A resistive version of the ideal force-free current density is used, (see equations 10 and 11 in Parfrey, Spitkovsky & Beloborodov 2017), given by

$$\begin{aligned} \frac{4\pi}{c}\mathbf{J} = [\boldsymbol{B}\cdot\nabla\times\boldsymbol{B} - \boldsymbol{E}\cdot\nabla\times\boldsymbol{E} + \gamma \boldsymbol{E}\cdot\boldsymbol{B}]\frac{\boldsymbol{B}}{(1+\gamma\eta)B^2} \\ +\nabla\cdot\boldsymbol{E}\frac{\boldsymbol{E}\times\boldsymbol{B}}{B^2+\tilde{E}^2}, \end{aligned} \tag{13}$$

With

$$\begin{aligned} \tilde{E}^2 &= \tilde{B}^2 + \mathrm{e}^2 - B^2, \\ \tilde{B}^2 &= \frac{1}{2}\left[B^2 - \mathrm{e}^2 + \sqrt{\left(B^2-\mathrm{e}^2\right)^2 + 4(\boldsymbol{E}\cdot\boldsymbol{B})^2}\right]. \end{aligned} \tag{14}$$

Here, η is the resistivity and γ is the driving rate. In this work, η is modelled as a constant and the value is kept very small. We set $\eta = 0.001$ and $\gamma = 250$.

The code uses spectral filtering to overcome the build-up of power at high wavenumbers and discontinuities generated due to non-linear coupling. The filter is given by

$$\sigma(\eta) = \mathrm{e}^{-\alpha\eta^{2p}}, \tag{15}$$

where $2p$ is the order of the filter and α characterizes the strength of the filter. The code uses two filters, a high order to prevent aliasing instability ($2p = 36$, $\alpha = 35$) and a lower order ($2p = 8$, $\alpha = 0.01$) super spectral viscosity (SSV) filter to provide some dissipation.

The simulation domain extends from $r_{\rm in} = r_\star$, the neutron star radius, to the outer boundary $r_{\rm out}$. We add an absorbing *sponge layer* near the outer boundary to absorb outgoing waves. One important characteristic spatial scale for a rotating system is the radius of the light cylinder $R_{\rm LC}$, given by the inverse of the star's unperturbed rotational angular velocity $R_{\rm LC} = 1/\Omega$. In this work, we concentrate on $R_{\rm LC} = 5$.

For both slow-shearing and fast-shearing simulation models, we performed the simulations with two sets of values for the outer boundary at $r_{\rm out} = 10 r_\star = 2R_{\rm LC}$, $100 r_\star = 20 R_{\rm LC}$. In the upcoming sections, we will refer to them as short-scale and long-scale simulations, respectively. We will focus on short-scale runs when we are interested in observing the behaviour of the magnetosphere near the

light cylinder whereas we will use long-scale runs when interested in studying the behaviour of the system away from the light cylinder.

For the flux tube simulations, however, we only performed simulation runs with the outer boundary fixed at $r = 100r_\star$. This is because we are mostly interested in analyzing the trajectory of the flux tube in the magnetospheric wind once the tube has been launched.

We use smooth coordinate mapping for the radial grid, while the grid is equispaced in θ direction. We use a non-uniform grid, which has very good resolution near the star, so code can resolve very fine details in the magnetosphere. The computational mesh consists of $N_r \times N_\theta$ cells in (r, θ) directions, respectively. We tested our code with various combinations of N_r, N_θ and found that a very high resolution is not needed to analyze the behaviour of our system. In Table 2, we describe the relevant simulation parameters for all three models. We ran all our simulation sets for at least over seven rotational periods. In sets where we suspected different behaviour at late time, the simulations were run over for a longer duration.

Our simulation region has two major boundaries: the inner boundary, i.e. the surface of the star and the outer boundary defined by the size of our simulation box. We assume axisymmetry as well as symmetry about the equatorial plane. The normal component of the magnetic field, B_r, and the tangential components of the electric field are continuous across the surface and therefore are known. The required boundary conditions at $r = r_\star$ are

$$\begin{aligned} B_r &= B_r(\theta), \\ E_\theta &= -\Omega B_r \sin\theta, \\ E_\phi &= 0. \end{aligned} \tag{16}$$

For CME ejection simulation, we introduce shearing after one rotation period by simply modifying the net angular velocity at the surface by $\Omega = \Omega_\star + \omega_s$.

3.2 Global magnetospheric structure

Investigations are done with the code PHAEDRA (Parfrey et al. 2012), Appendix 3.1. We have verified that for non-sheared configurations, our procedure reproduces the analytical solution and key known results (e.g. formation of plasmoids at the Y-point), see Appendix B.

The first important ingredient that affects the generation of flares is the global structure of the magnetosphere. To investigate the influence of global magnetic structure on the generation of CMEs, we first consider several initial magnetospheric configurations: purely dipole, twisted dipole-like configurations, dipole+quadrupole, and dipole + octupole fields.

The expressions for magnetic fields of dipole, quadrupole, and octupole, normalized with respect to the field at the pole B_p is given by

$$\begin{aligned} \boldsymbol{B}_d &= \left\{\cos\theta, \frac{\sin\theta}{2}, 0\right\} B_p \frac{R^3}{r^3}, \\ \boldsymbol{B}_q &= \left\{\frac{1}{4}(3\cos(2\theta)+1), \sin(\theta)\cos(\theta), 0\right\} B_p \frac{R^4}{r^4}, \\ \boldsymbol{B}_o &= \left\{\frac{1}{2}(5\cos(\theta)^2-3), \frac{3}{4}\sin(\theta)(5\cos(\theta)^2-1), 0\right\} B_p \frac{R^5}{r^5}, \\ \boldsymbol{B}_{tot} &= \boldsymbol{B}_d + \mu_{q,o}\boldsymbol{B}_{q,o}. \end{aligned} \tag{17}$$

See Appendix A for a more detailed description of the analytically tractable case of dipole + quadrupole configuration.

We then study three different configurations: (i) dipole; (ii) mixed dipole–quadrupole; and (iii) mixed dipole–octuple. The relative strength of the higher multipoles is parameterized by μ_q and μ_o. In what follows, we use $\mu_q = 2$ and $\mu_o = 3$ – in these cases, the higher order multipoles introduce non-trivial corrections to the surface fields if compared with dipolar (e.g., in the case of dipole–quadrupole configuration, a 'dome' appears near the south pole), see Figs 2 and A1.

Table 2. Table showing simulation parameters for the models used in this work.

Model	r_{out}	$N_r \times N_\theta$
Slow shearing	10,100	280 × 180
Fast shearing	10,100	260 × 200
Flux tube	100	340 × 220

3.3 Prescriptions for foot-point shear

The second important ingredient is the location of the shear. The imposed shear on magnetic foot-points is confined to a small band, to be located at various latitudes and of latitudinal extent. The shearing is applied at the inner boundary of our simulation, the radius of the star.

When the two foot-points of the sheared arcade are well separated, we employ symmetric shear, moving azimuthally only one set of footprints (This is nearly equivalent to antisymmetric shear, when the two footprints are moved in the opposite direction, given the overall spin of the star). The symmetric shear fails to create an expanding flux tube for the case of equatorial shear – in that case, symmetric shear moves both footprints in the same direction so that the global magnetosphere can remain stationary (Lyutikov & Sharma 2022). To induce explosion for the equatorial shear, we apply antisymmetric prescription, equation (20).

We employ several prescriptions for symmetric shear. First, we follow the discussion in section 3 of Antiochos et al. (1999). The angular velocity of the foot-points ω_s is (see Fig. 3)

$$\omega_s(\theta) = \begin{cases} \omega_{max} g(\theta), & \text{for } \theta_{band} - \Theta \le \theta \le \theta_{band} \\ 0, & \text{otherwise}. \end{cases} \tag{18}$$

Here, ω_{max} is the maximum value of applied shear, and function $g(\theta)$,

$$\begin{aligned} g(\theta) &= C\left(\psi^2 - \Theta^2\right)^2 \sin\psi \\ \psi &= \theta_{band} - \theta, \end{aligned} \tag{19}$$

defines the latitudinal extent of the shear region, and θ_{band} is the polar angle around which shearing is applied. C is a normalization constant introduced to ensure that $\max|g(\theta)| = 1$ and $\Theta = \pi/15$ is the assumed latitudinal extent of the shear layer.

We can also construct an expression for antisymmetric shearing as follows:

$$\omega_s(\theta) = \begin{cases} \omega_{max} g(\theta), & \text{for } \theta_{band} - \Theta \le \theta \le \theta_{band} + \Theta \\ 0, & \text{otherwise}. \end{cases} \tag{20}$$

Since for the rotating case, we are mostly interested in the ratio of shear velocity to the stars rotation velocity, we rearrange equation (18), to get

$$\frac{\omega_s}{\Omega_\star} = \begin{cases} \xi\, g(\theta), & \text{for } \theta_{band} - \Theta \le \theta \le \theta_{band} \\ 0, & \text{otherwise}. \end{cases} \tag{21}$$

Where $\xi = \omega_{max}/\Omega_\star$.

The shear profile for both symmetric and antisymmetric cases, as the function of θ, is plotted in Fig. 3 for three different locations of the shearing band.

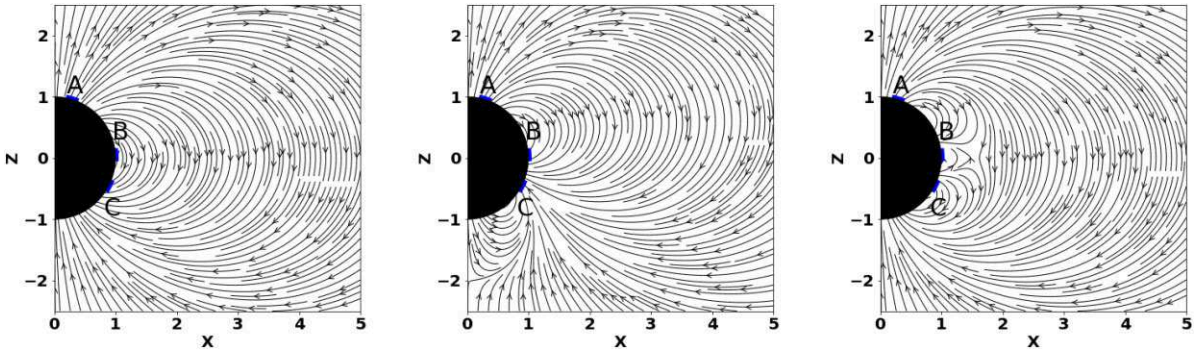

Figure 2. Initial poloidal field lines for superposition of dipole, dipole plus quadrupole, and dipole plus octupole (left- to right-hand panels) for $\mu_q = 2$ and $\mu_o = 3$, see equation (17). Shearing regions A, B, and C are at 20°, 90°, and 120°, respectively, from the z-axis. Here and below scales are normalized to neutron star radius.

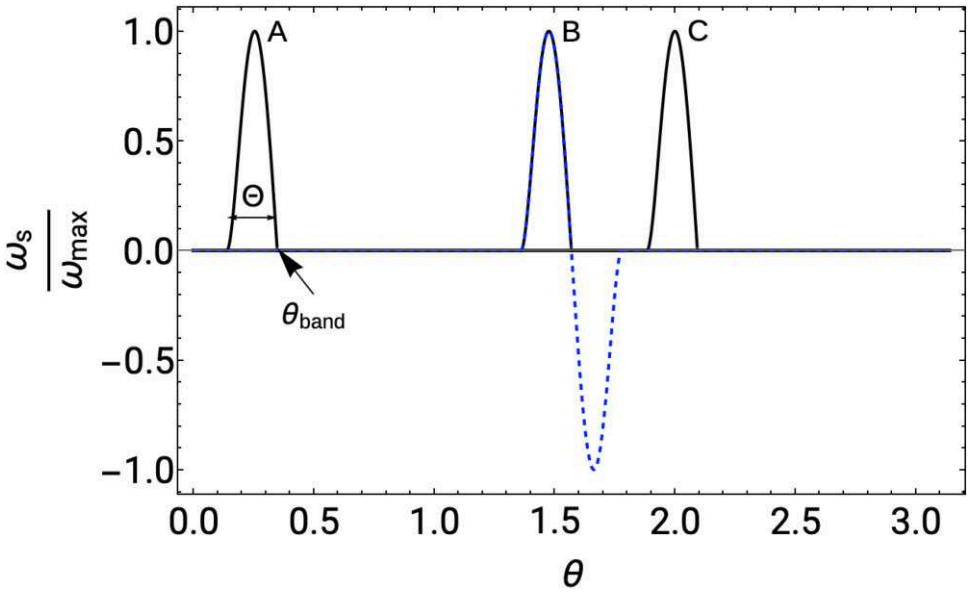

Figure 3. Normalized shear velocity (ω_s/ω_{max}) as a function of co-altitude θ (see equations 18 and 20). Solid black curves show the shear profile for the symmetric mode at three different regions (A, B, and C), whereas the blue-dashed line represents the shear profile for the antisymmetric mode near the equator (region B).

4 CORONAL MASS EJECTIONS DEEP INSIDE MAGNETOSPHERES

4.1 Sheared non-rotating magnetospheres

We start this work by probing static non-rotating configurations with shearing introduced at different locations. The main justification is the limited dynamic range of simulations of the rotating magnetospheres, Section 5. Our typical light cylinder radius is only five stellar radii, while in the case of a magnetar, the expected ratio is in the tens of thousands (for ∼1 s period).

As a key new ingredient, we probe the effect of various magnetic field topologies by adding contributions from other multipoles. We achieved this by superimposing quadrupole and octupole fields on the star's dipolar field (see Section 3.2). Since we are mostly interested in the CME ejections, we chose a relatively high shearing rate to ensure the magnetosphere enters into a non-equilibrium dynamic state (Mikic & Linker 1994; Parfrey, Beloborodov & Hui 2013). For this and the subsequent simulations, the maximum shearing rate ω_{max} was chosen as 0.1 (so that the light cylinder corresponding to the shearing motion is at 10 stellar radii.)

The shearing of foot-points starts immediately at the beginning of simulations $t = 0$, causing the field lines to twist. The subsequent evolution of the system is visualized in Fig. (4), where we plot toroidal current density J_ϕ for the combination of different shearing altitude and magnetic field topology, for short scale runs ($r_{out} = 10$). To demonstrate the importance of the location of foot-point shearing, we consider three different shearing regions: near the poles (region A), at the equator (region B), and at ∼120° from the poles (region C).

No ejections were seen when the shearing region is located near the poles (Region A) for all three initial magnetic field topologies. As observed in Fig. 4, left-hand panel, there is not a substantial poloidal expansion, and the system attains a quasi-equilibrium state where most of the field lines remain closed.

For the case of equatorial shearing (region B), we see major explosive events for the superposition of dipole and quadrupole/octupole topologies. We attribute this to the significant opening of the closed lines. While the ejection is evident for the case of dipole and octupole superposition, we show the final inflated state for the remaining two configurations: the structure breaks away and exits the simulation box at the next time-step. This equatorial expansion is consistent

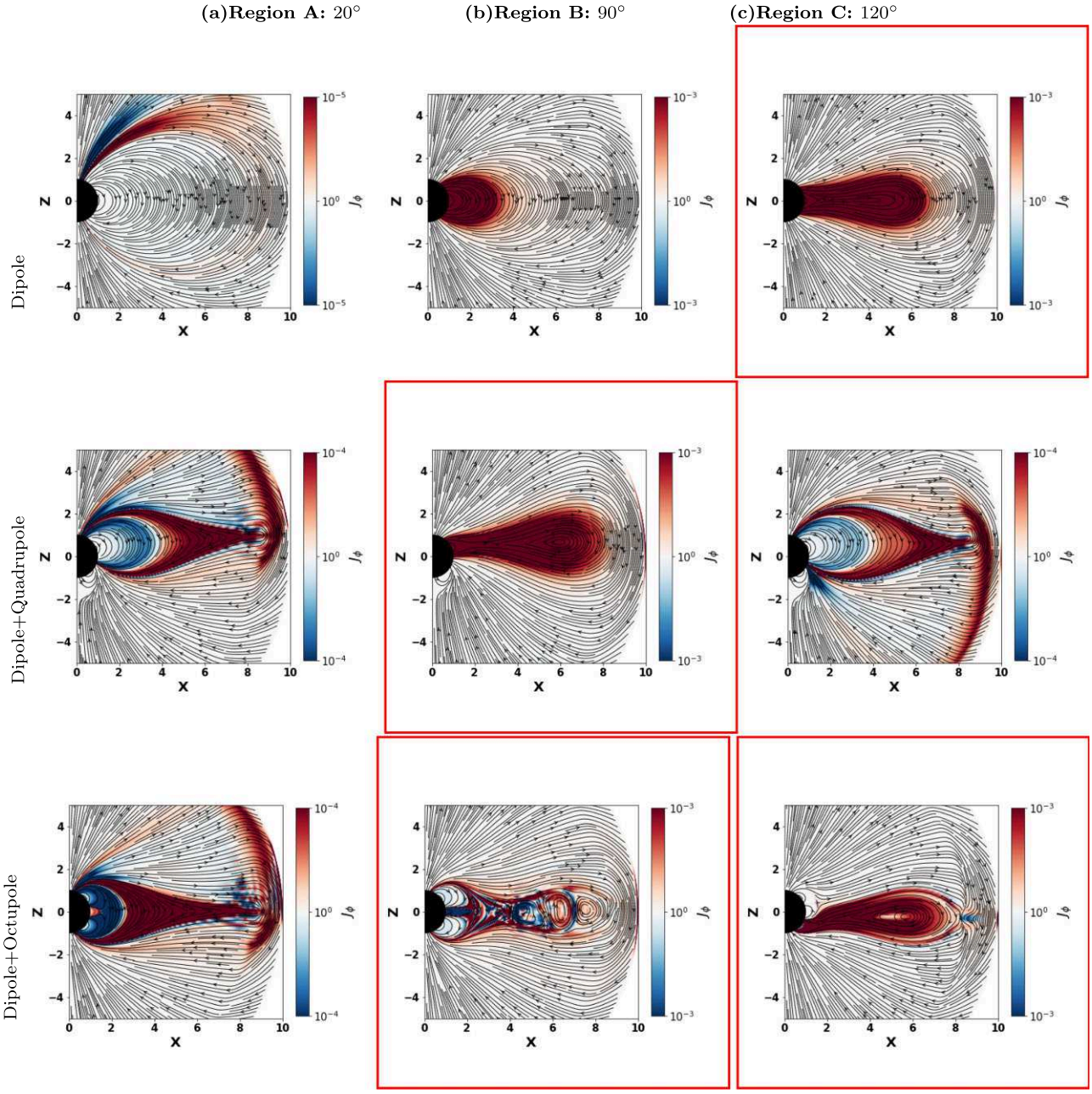

Figure 4. Toroidal current density(J_ϕ) for non-rotating configurations sheared at various altitudes (20°, 90°, and 120° from the left- to the right-hand panels, respectively). Shearing rate is $\omega_{\max} = 0.1$. The computational domain extends till 10 stellar radius ($r_\star$). In all cases, when shearing is done close to the north pole (region A, left-hand column), no major ejection events are observed. When shearing near the equator (region B, middle column) or region C (right-hand column) whether or not ejections are observed depends on the magnetic field topology. Red boxes are drawn around configurations where a clear expulsion of plasmoids is observed.

with previous simulations by other authors (Mikic & Linker 1994; Parfrey et al. 2013). As argued in above-mentioned works, field line opening causes the formation of a current sheet, and the subsequent reconnection of field lines triggers the ejection of magnetic energy in the form of CMEs.

The ejections profile while shearing region C, however, depends on the magnetic topology, as depicted in Fig. 4 right-hand panel. Unlike in the case of dipole and dipole+octupole magnetosphere, the field lines for dipole + quadrupole topology are only partially open and the system achieves a quasi-equilibrium state. In Fig. 4, we highlight those cases where the system explodes and ejects CMEs with a red box. For the rest of the cases, no emissions were observed within the temporal limit of our simulation.

We further show the large-scale time-evolution of two selected configurations: dipole + quadrupole and dipole sheared antisymmetrically in Fig. 5. We see ejection events in both scenarios, albeit at different times. In Fig. 6, we zoom in on Fig. 5(e) to highlight the structure of the exploded shell – most of the energy/magnetic

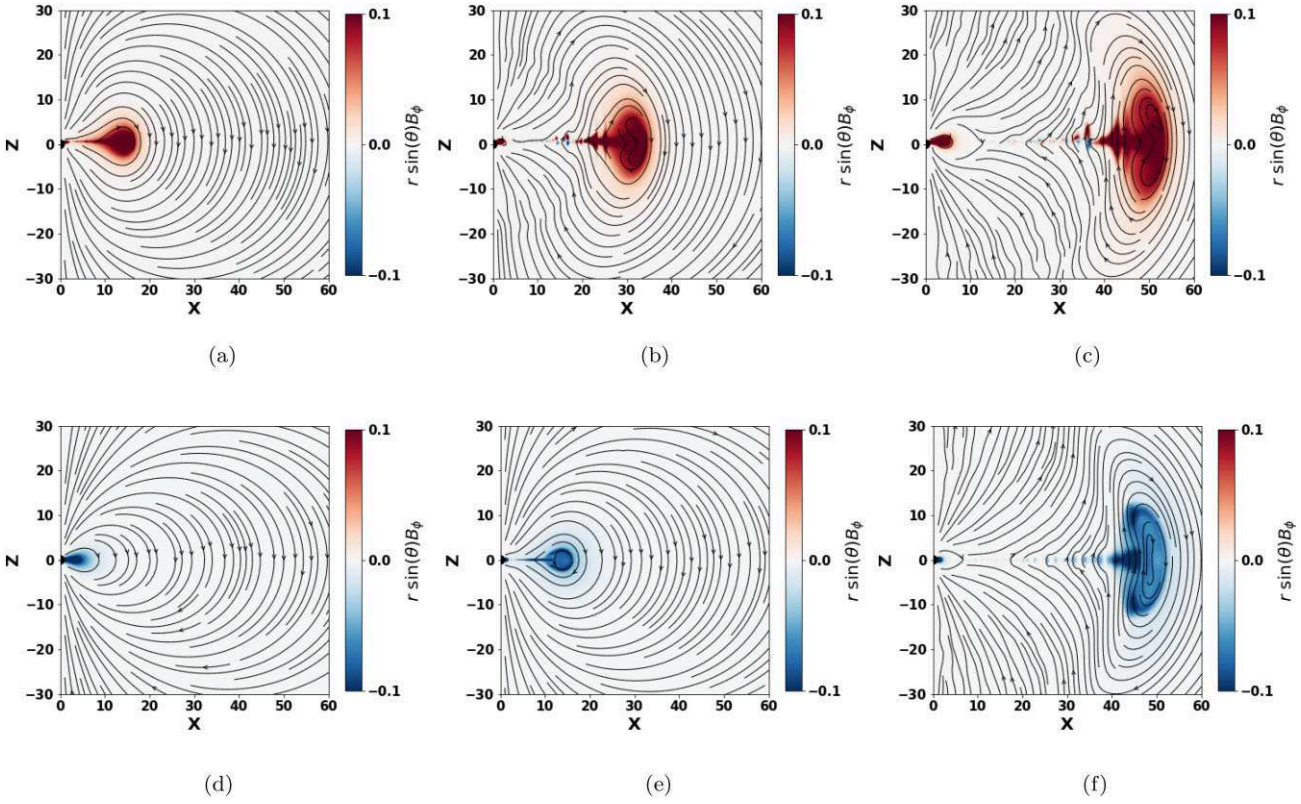

Figure 5. Time evolution for non-rotating dipole + quadrupole sheared at point B (top panel), and dipole sheared antisymmetrically at point B (bottom panel), for large-scale run. Colour is the toroidal magnetic field $r\sin(\theta)B_\phi$ (this applies to other figures unless stated otherwise), and streamlines are poloidal fields. Shearing starts at the beginning of the simulation.

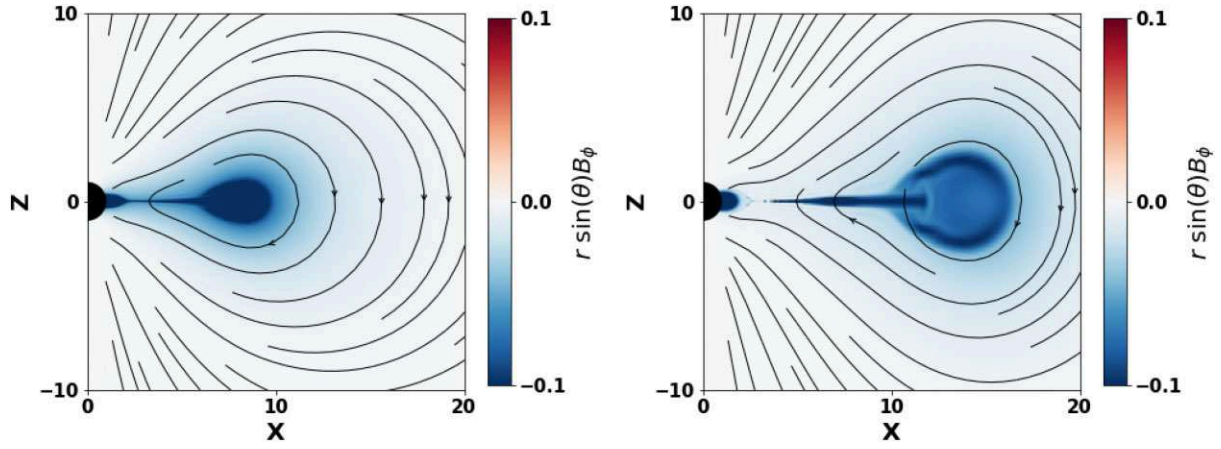

Figure 6. Detonating CME within the magnetosphere. Right-hand panel: zoomed-in version of Fig. 5(e): notice the edge-enhances structure of the detonating CME, cf. Fig. 1. As discussed by Barkov et al. (2022), detonating magnetic structures are concentrated near the surface. Left-hand panel: we show the system approximately a third of a period before the detonation.

field is concentrated near the surface of a detonating flux tube as discussed/simulated by Barkov et al. (2022). Numerically, we verified that the detonation occurs approximately at (8). Precise location/confirmation suffers from the facts that the external energy scales as $r_{\rm eq}{}^{-3}$, so that the error in the estimate of $r_{\rm eq}$ from simulations by a factor of 2 (due to the finite size of the flux tube and not a strict definition of the detonation moment) leads to large variation in the value of the external energy.

5 CORONAL MASS EJECTIONS BY ROTATING MAGNETOSPHERES (SLOW SHEAR)

5.1 Results: magnetospheric dynamics for slow shear

Next, we proceed to the main topic of this paper: dynamics of CMEs in relativistic rotating magnetospheres with sheared foot points. For slow shear, we set $\omega_{\rm max} = 0.1$, which corresponds to $\xi = 0.5$ (maximal shearing rate is half the spin). The shearing of the stellar surface

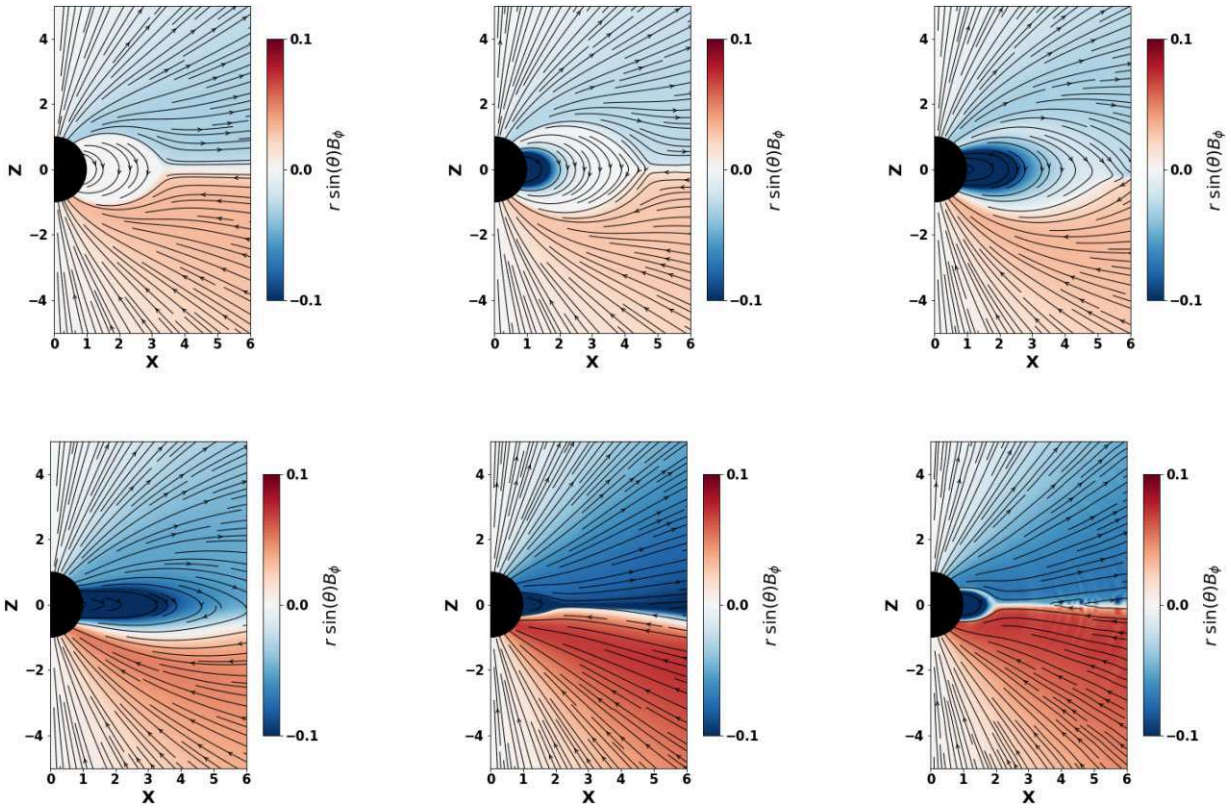

Figure 7. Time-evolution for rotating dipole configuration sheared antisymmetrically at point B (equatorial), slow shear. The computational domain extends till 10 stellar radius ($r_\star$). Snapshots are taken at $t = \{0.95, 3.2, 5.4, 6.4, 7.0, 7.3\}$. Shearing starts at $t = 1$ (after one rotation period). One can clearly observe the opening of the field line and ejection of a CME. After the CME is ejected, the closed part of the magnetosphere is smaller, with the current sheet showing plasmoid instability. The final configuration has a non-zero twist on closed field lines – compare the first and last panels. See also Fig. 12 for the large-scale dynamics.

begins after one rotational time period, to ensure that our initial unsheared system is in an equilibrium state.

We start with the basic case of dipolar magnetosphere sheared at the equator with an antisymmetric shearing profile (20), Fig. 7. We introduce magnetic foot-point shearing to rotating neutron stars. One can clearly observe the opening of the field line and ejection of a CME. After the CME, the closed part of the magnetosphere is smaller, with the current sheet showing plasmoid instability. The final configuration has a non-zero twist on closed field lines.

The behaviour matches the expectations: the closed field lines become partially or even fully opened in response to finite foot-point shearing due to additional magnetic pressure from the toroidal component of the magnetic field (Wolfson & Low 1992). The opened field lines subsequently cause the expulsion of magnetic energy in the form of CMEs.

The post-CME relaxation is a new effect: formation of a smaller closed magnetosphere, with a plasmoid-mediated current sheet deep inside the light cylinder, and a slow, reconnection-mediated relaxation to a new equilibrium with twisted field lines.

Though our force-free simulations are not designed to catch resistive-type plasmoid instability, experience tells us that numerical resistivity in many cases mimics surprisingly well the qualitative details of real resistivity, including plasmoid instability (e.g. Komissarov et al. 2007; Lyutikov & McKinney 2011; Parfrey et al. 2013; Del Zanna et al. 2016; Ripperda et al. 2019). Realistic relativistic reconnection in current sheets forms series of plasmoid islands, which allows forming fast reconnection regime with reconnection speed about 0.1c. The last statement was confirmed by PIC simulation and two-fluid simulations as well (Barkov & Komissarov 2016). Also, two-fluid simulations show significant rate of the reconnection with gas pressure as well with strong guiding field (see the paper above and some unpublished results, which is in a good agreement with PIC results). So the relativistic fast reconnection is feasible, and our fast reconnection also mimic realistic reconnection process.

Next, we show the time-evolution of sheared dipole and quadrupole systems for equatorial shearing in Fig. 8, left-hand column. The opening of field lines and subsequent ejection of CME is clearly evident. In Fig. 8, we compare the dynamics of the same configuration (dipole + quadrupole configuration sheared at point B), between rotating and non-rotating cases. We clearly see that it is much easier to break out from the rotating magnetosphere. This is expected since in the rotating case the breakout occurs when the top of the inflated loop reaches the light cylinder. Fig. 8 also demonstrates that though our dynamic range is not very large (light cylinder at only five stellar radii), we do correctly capture the dynamics of the inflated flux tube within the magnetosphere.

Finally, in Fig. 9, we discuss all three magnetic configurations sheared at various locations. The top panel shows systems with only dipolar fields. No ejections were observed when shear was applied near the polar area (region A) and the system remained in a quasi-equilibrium state. Similar to what we observed in the previous section for non-rotating systems, this observation will hold true even for more complicated magnetic topologies. We also don't observe ejections while shearing near the equator (region B). This is

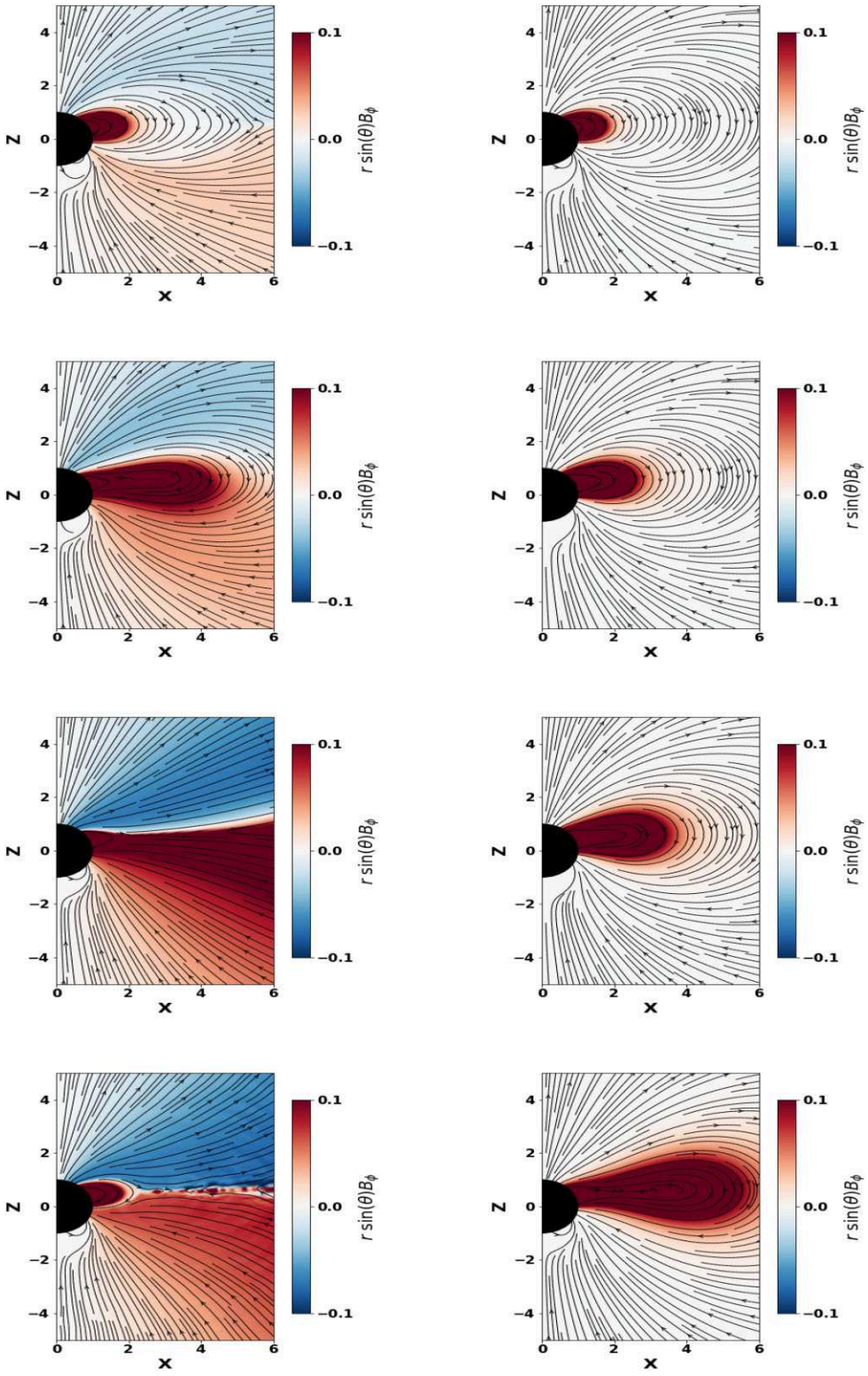

Figure 8. Dipole + quadrupole configuration sheared at point B (equatorial), slow shear. The computational domain extends till 10 stellar radii ($r_\star$). Left-hand column: rotating case, right-hand column: non-rotating case (snapshots are taken at the same time, as measured from the start of the shearing). One clearly sees the influence of the light cylinder on the development of the CME. This demonstrates that the light cylinder makes it 'easier' for the CME to break out.

a consequence of the fact that our shearing profile is symmetrical i.e. for the equatorial case, the shearing is confined to one hemisphere.

In the middle panel, we consider a rotating star system with superposition of dipole and quadrupole field, we find that powerful ejection events are observed when shearing between $\sim 30^\circ$ and 100°. This is consistent with our hypothesis that strong ejections are observed while shearing regions with closed field lines (bigger loop in Fig. 10). We demonstrate our results by plotting the toroidal current

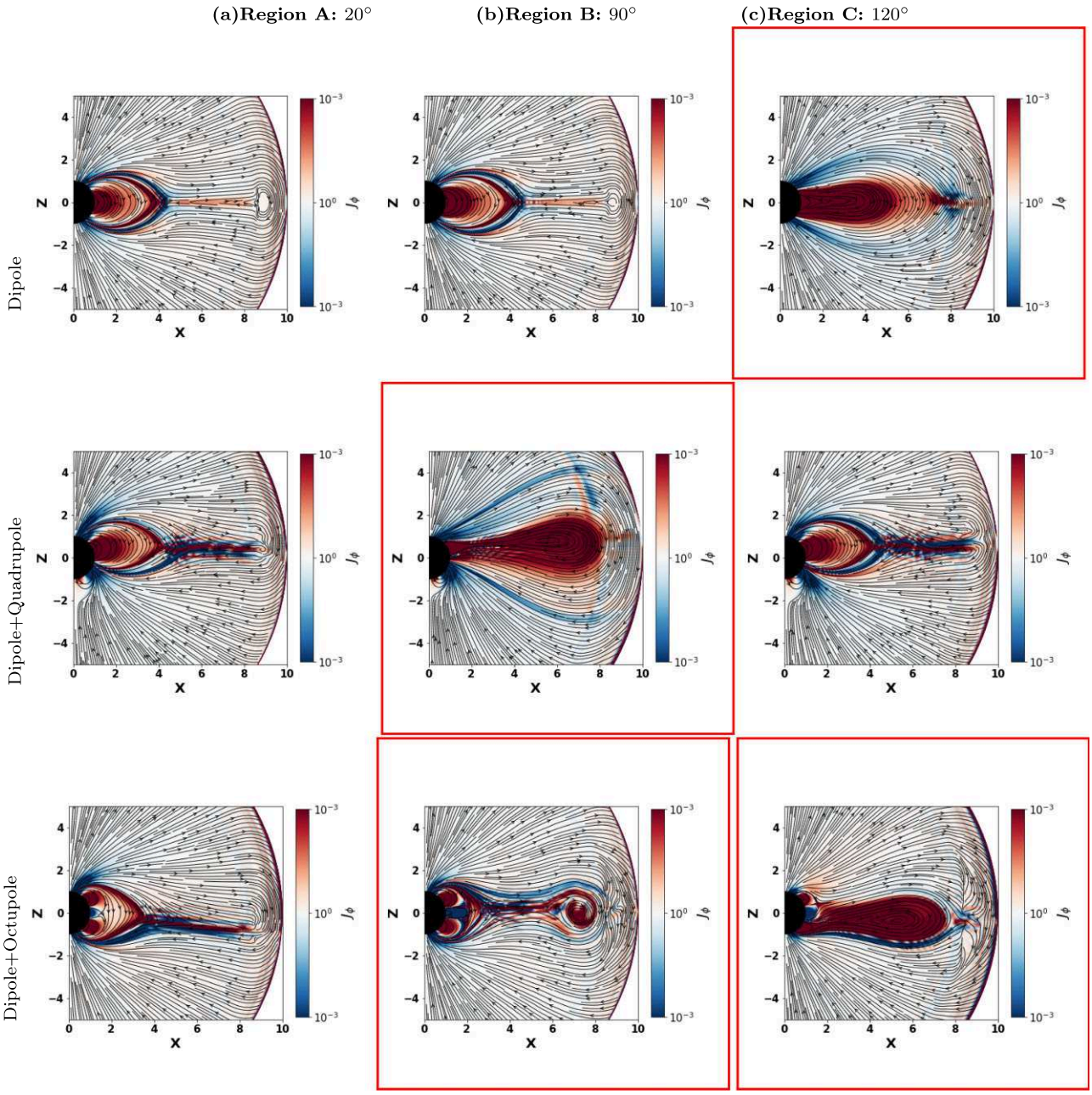

Figure 9. Toroidal current density J_ϕ for rotating and sheared configurations. The computational domain extends till 10 stellar radii ($r_\star$). Overall angular velocity of the star is $\Omega = 0.2$ (so that the light cylinder is at $x = 5$), normalized shear parameter $\xi = 0.5$ (so that maximal shearing angular velocity is $\omega_{\max} = 0.1$), symmetric shear (so that all foot-points are moved in the same azimuthal direction). In all cases, when shearing is done close to the north pole (region A, left-hand column), no major ejection events are observed. When shearing near the equator (region B, middle column), in all cases, we observe powerful ejections. When shearing is done at region C (right-hand column) whether or not ejections are observed depends on the magnetic field topology: In the Dipole + Quadrupole case (second row, right-hand column), no powerful ejections are observed. Red boxes are drawn around configurations where a clear expulsion of plasmoids is observed.

at three different locations: near the poles (region A), at the equator (region B), and at $\sim 120^\circ$ from the poles (region C). In the bottom panel, we consider simulations with the superposition of dipole and octupole fields. Powerful plasmoid ejection events are observed once the shearing region is away from the polar region.

Based on the above results, we can safely conclude that the effects of shearing highly depend on how far the field lines extend. Shearing closed field lines leads to powerful ejections whereas if the shearing region is located in an area where field lines have started opening out, no or weak pulsating ejections are observed. Following the discussion in Section 4.1, we highlight those cases where the explosion can be observed with a red box. In Table 3, we summarize our results for rotating sheared configurations (see also Section 6.4 for a related case of fast shear).

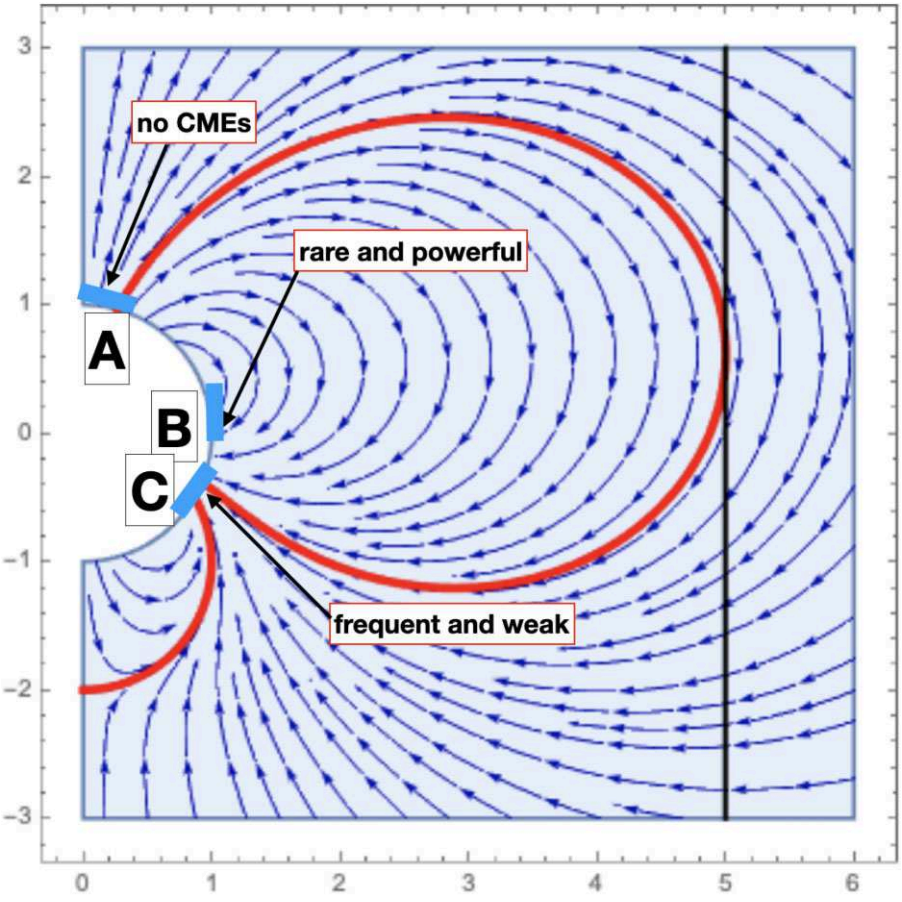

Figure 10. Qualitative description of flare dynamics depending on the location of the shear (dipole–quadrupole case). The vertical line at 5 is light cylinder.

Table 3. Table summarizing results from simulations when the magnetic field lines are sheared for rotating stars, following the prescription in Antiochos et al. (1999).

Field topology	Shearing region		
	Region A	Region B	Region C
Dipole	Weak pulsating eruptions (Fig. 9a, top panel)	Weak pulsating eruptions (Fig. 9b, top panel)	Powerful ejections (Fig. 9c, top panel)
Dipole + quadrupole	Weak pulsating eruptions (Fig. 9a, middle panel)	Few but powerful (Fig. 9b, middle panel)	Weak pulsating eruptions (Fig. 9c, middle panel)
Dipole + octupole	Weak pulsating eruptions (Fig. 9a, bottom panel)	Frequent and powerful (Fig. 9b, bottom panel)	Frequent and powerful (Fig. 9c, bottom panel)

5.2 Conclusion 1: three important ingredients for the generation of CME: global magnetospheric structure, location of foot-point shear, and rotation

Different magnetic field configurations are required for CME initiations by different models (Li & Luhmann 2005). The *Break-out* model proposed by Antiochos et al. (1999) has a multiflux topology with four distinct flux systems. The shearing of the central arcade (which straddles the equator) and the subsequent reconnection of the sheared magnetic arcade with the overlying unsheared field leads to the build-up of large energy excess in closed sheared field lines, to power CME.

Another similar model was proposed by Mikic & Linker (1994), where the trigger for plasmoid ejections is the introduction of resistivity in the plasma when the shearing is turned off. The introduction of resistivity causes the magnetic field lines to reconnect in the current and the subsequent formation and ejection of plasmoid islands. In the absence of plasma resistivity, no eruption occurs, field lines become fully opened and the system remains in equilibrium.

The major difference between this work and the model by Antiochos et al. (1999) is the inclusion of the rotation of the star. The rotation of the star, which, in turn, leads to the formation of the light cylinder, removes the need for magnetic reconnection. The flux tube opens up to infinity approximately when the top point reaches the light cylinder.

We find a relatively simple picture of shear-generated explosion: the location of the shear for a given global magnetospheric structure determines the presence or absence of strong ejection events. Qualitatively, we show the results for dipole + quadrupole configuration in Fig. 10.

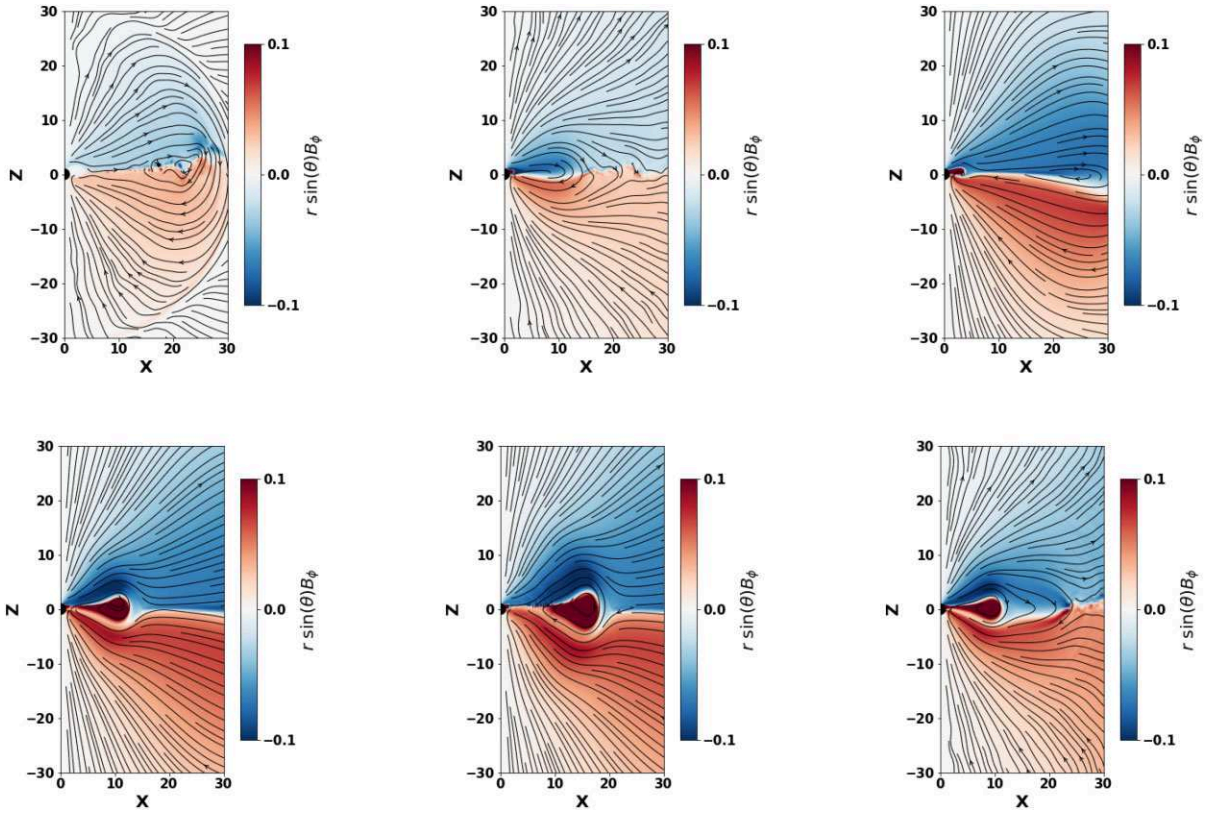

Figure 11. Rotating dipole + quadrupole configuration sheared at point B (equatorial), slow shear for the large-scale run. The computational domain extends till 100 stellar radius ($r_\star$), although here we zoom-in till $r = 30r_\star$. The snapshots are taken at $t = 0.99$, 2.4, 3.2, 3.6, 3.8, and 5.3 of the rotational period of the star. Shearing is introduced after one rotation. One can clearly observe the opening of the field line and ejection of a CME. After the CME, the closed part of the magnetosphere is smaller, with the current sheet showing plasmoid instability. The final configuration has a non-zero twist on closed field lines.

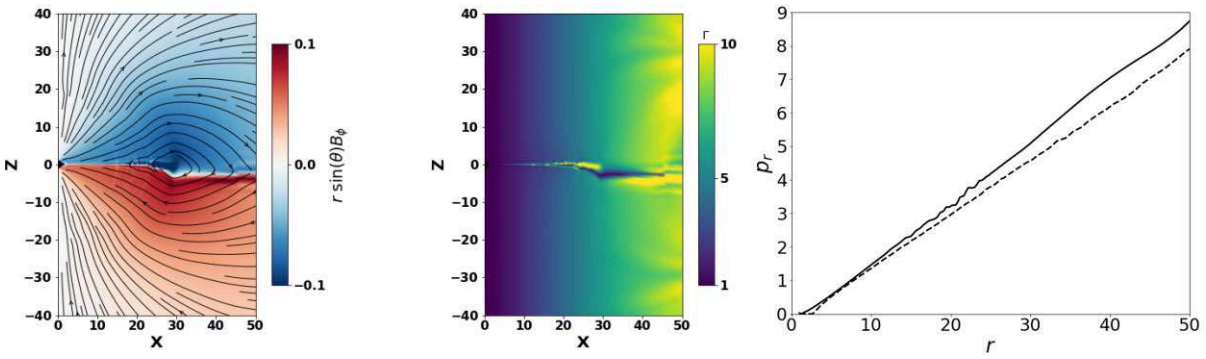

Figure 12. Similar to Fig. 7 (dipolar field sheared antisymmetrically at region B) but on large scales. Plotted are values of $r\sin\theta B_\phi$ (left-hand panel), Lorentz factor (middle panel) and radial momentum $p_(r)$ as a function of radial distance r at a zenith angle of 60° from the pole for the above configuration (solid) and for unsheared rotating dipolar configuration (dashed). The snapshots are taken at $t = 7.8$. As observed from the middle and left plots, there is minimal effect of the ejection on the Lorentz factor Γ.

5.3 Large-scale dynamics of ejected CMEs in the wind, and conclusion 2

Previously, in Section 5.1, we discussed the generation of a CME within the magnetar's magnetospheres. Next, we study the large-scale dynamics of the resulting CME. We start with a large-scale simulation showing the time-evolution of a sheared dipole + quadrupole configuration, see Fig. 11. Here, we set the outer boundary far away from the light cylinder, $r_{\rm out} = 20r_{\rm LC}$.

In Figs 12 and 13, we plot a large-scale snapshot for the two cases of dipolar fields sheared antisymmetrically and dipole plus quadrupole configuration sheared at point B.

Recall that shearing results in the generation of a topologically disconnected flux tube, a CME. In Figs 12 and 13, an ejected CME is clearly identified in the left-hand panels around $x \approx 25$. At the same time, the CME is barely seen in the Lorentz factor/radial momentum plots (centre and left-hand panels): topologically disconnected CME

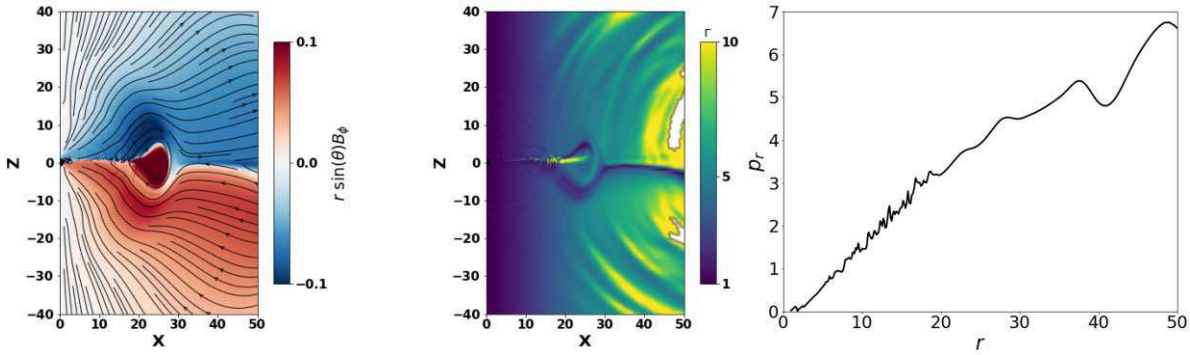

Figure 13. Similar to Fig. 11 (dipole + quadrupole configuration sheared at point B) but here we show Lorentz factor Γ and radial momentum p_r as a function of radial distance r at a zenith angle of 60° from the pole along with scaled toroidal magnetic field at $t = 4.1$. As observed from the middle and left-hand plots, there is minimal effect of the ejection on the Lorentz factor Γ.

is frozen into the wind and propagates with the local Lorentz factor of the wind.

Overall, our numerical results are in excellent agreement with analytics (Lyutikov 2022), see Fig. 1.

6 GLITCHED MAGNETOSPHERE (FAST SHEAR)

6.1 Magnetar's CMEs in the *Star Quake* paradigm

In a complementary approach, which can be supported by a fully analytical model, we consider a model of propagation of the force-free electromagnetic pulse generated by a sudden *local* spin-up of a neutron star, a 'Glitched Magnetosphere'. This type of dynamics mimics the starquake model of Thompson & Duncan (1995) and Yuan et al. (2020)

6.2 Locally glitched Michel's magnetosphere: analytical approach

Effects of 'glitch in spin' on the structure of the wind can actually be considered analytically and non-perturbatively for the case of Michel (1973) magnetospheres and the preceding wind:

$$\begin{aligned}
\boldsymbol{B} &= B_0 \left\{ \frac{r_0^2}{r^2}, 0, -\frac{r_0^2 \Omega \sin(\theta)}{r} \right\}, \\
\boldsymbol{v} &= \left\{ \frac{r^2\Omega^2 \sin(\theta)^2}{1 + r^2\Omega^2 \sin(\theta)^2}, 0, \frac{r\Omega \sin(\theta)}{1 + r^2\Omega^2 \sin(\theta)^2} \right\}, \\
\boldsymbol{\Gamma} &= \sqrt{1 + r^2\Omega^2 \sin(\theta)^2}, \\
\boldsymbol{p} &= \left\{ \frac{r^2\Omega^2 \sin(\theta)^2}{\sqrt{1 + r^2\Omega^2 \sin(\theta)^2}}, 0, \frac{r\Omega \sin(\theta)}{\sqrt{1 + r^2\Omega^2 \sin(\theta)^2}} \right\}.
\end{aligned} \tag{22}$$

B_0 is the fiducial magnetic field magnitude at the light cylinder (r_0) and we set $c = 1$. Realistic dipolar magnetospheres do evolve asymptotically to the Michel (1973) solution (Bogovalov 1999; Contopoulos, Kazanas & Fendt 1999; Komissarov 2006).

One can generalize Michel's solution for any arbitrary time- and angle-dependent rotation $\Omega = \Omega[r - t]g(\theta)$ (Lyutikov 2011) (see also Gralla & Jacobson 2014). The solution can also be generalized to Schwarzschild metric using the Eddington–Finkelstein coordinates, Lyutikov 2011. This *glitch in spin* time-dependent non-linear solution (non-linear both in the sense that the current is a non-linear function of the magnetic flux function, and that the perturbation can be of large amplitude) preserves both the radial and θ force balance. Qualitatively, 'a glitch' in the angular rotation velocity Ω mimics a symmetric shearing motion of a patch of field lines (we remind: 'symmetric' means overall motion in one direction along ϕ). Approximation of Michel (1973) magnetospheres misses the magnetospheric dynamics, but it captures the wind dynamics.

In Fig. 14, we show the evolution of single Alfvén pulse using $g(\theta) = \sin^{10}(\theta + \pi/4)$ and $\Omega = 1 + \mathrm{e}^{-(r-t)^2}$. To complement the analytical work, we show the complete evolution of a pulse via numerical simulation in Section 6.3

A pulse of shearing Alfvén waves with $\Omega[r - t]g(\theta)$ propagates with radial 4-momentum

$$p_r = \frac{r^2 \sin^2\theta \Omega^2 [r - t] g(\theta)^2}{\sqrt{1 + r^2 \sin^2\theta \Omega^2 [r - t] g(\theta)^2}}, \tag{23}$$

which is larger than that of the wind for $\Omega[r - t]g(\theta) \geq \Omega_0$, the constant value. Higher radial momentum (than that of the background flow) *does not mean* that plasma is swept-up: It is just an EM pulse propagating through the accelerating wind.

Finally, we note that a glitch in fact can be local, with arbitrary ϕ-dependence (but only in the ϕ direction, Appendix C. Also, interaction with the current sheet (reversal of B_r) breaks the non-linear solution and will likely will lead to dissipation.

6.3 Locally glitched magnetosphere: simulations with PHAEDRA

In a numerical implementation, we limit ourselves to just dipolar magnetospheres. We use glitch parametrization as

$$\Omega = \Omega_0 \left(1 + g(\theta) f(t) \frac{\delta\Omega}{\Omega_0} \right). \tag{24}$$

Several types of shearing were implemented: (i) overall glitch $g(\theta) =$ constant (so, in this case, the glitch is actually global); (ii) symmetric $g(\theta) = \sin^{10}(\theta + \pi/4)$; (iii) and antisymmetric near the equator $g(\theta) = \sin^3(\theta)\cos(\theta)$. The extra rotation within the shearing band is fast $\delta\Omega/\Omega_0 = 5$.

Time dependence of the glitch is

$$\begin{aligned}
f(t) &= \sin[\pi(t - t_{\rm on})/\tau], \\
t_{\rm on} &= P \text{ (one period)}, \\
\tau &= P/10, \\
t_{\rm off} &= t_{\rm on} + \tau,
\end{aligned} \tag{25}$$

so that the glitch is implemented after one rotation for one-tenth of the with maximum rate reached when $t = t_{\rm on} + \tau/2$. Thus, a total

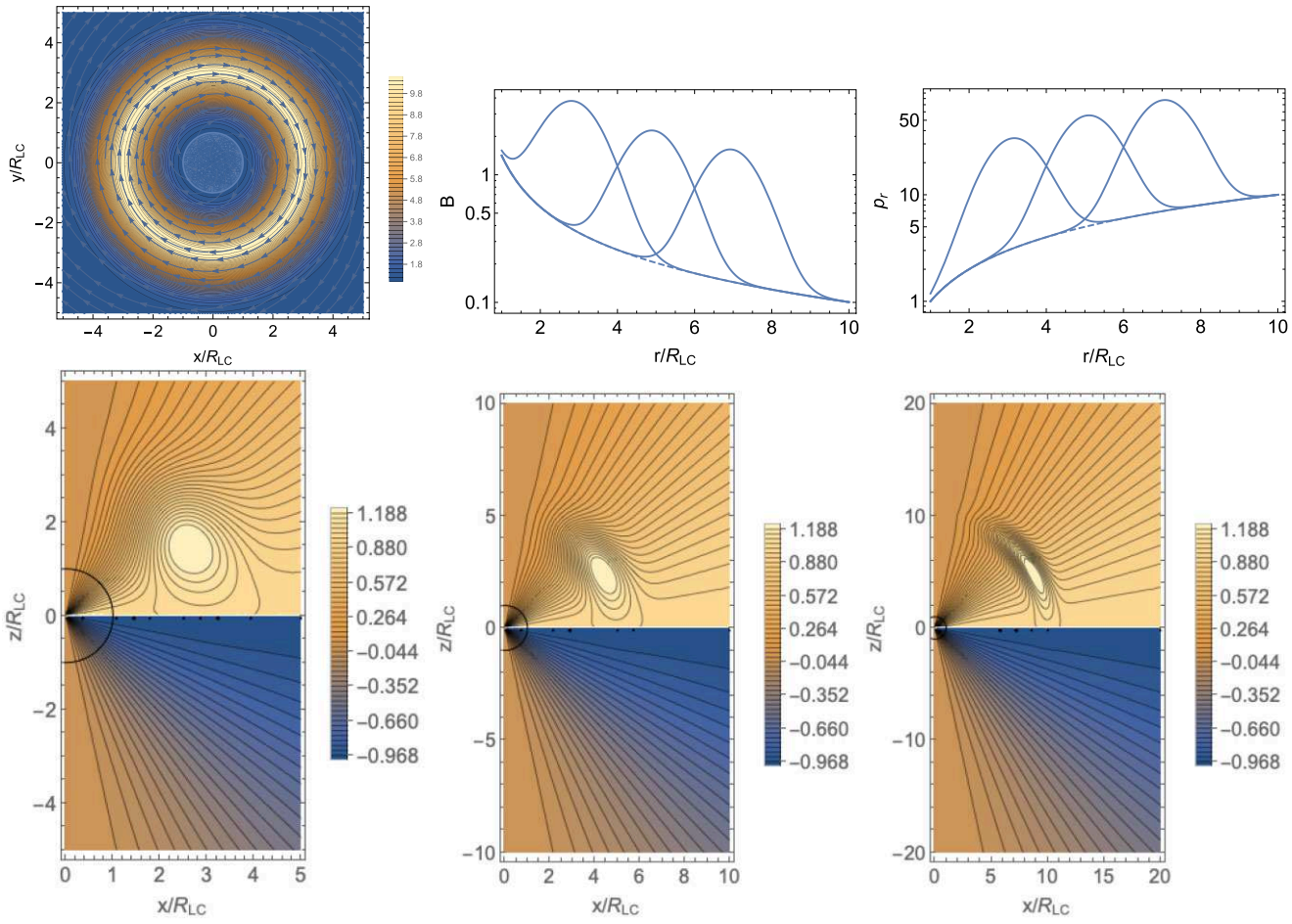

Figure 14. Top row – left-hand panel: structure of the magnetic field in the equatorial plane of an electromagnetic Gaussian pulse with amplitude 10 times the average propagating through Michel's wind. The peak of the pulse is at $r/R_{\rm LC} = 3$. The light cylinder is at $\sqrt{x^2+y^2} = 1$. The colour scheme corresponds to $\ln B/B_{\rm M}$, where $B_{\rm M}$ is the local value of the magnetic field for Michel's solution. Centre panel: plot of B showing EM pulse propagating with the wind for times $t = 3$, 5, and 7 (in units of $R_{\rm LC}/c$); dashed line is the Michels' solution. Right-hand panel: plot of $p_r(r)$. The pulse propagates with the flow with constant relative amplitude, without experiencing any distortions. Bottom row: value of $r\sin\theta B_\phi$.

shearing angle is $\Delta\phi = \pi$. Note that the shearing expression $g(\theta)$ used in this section is somewhat different from the one used for slow shearing.

6.3.1 *Overall glitch*

We first consider the case of constant $g(\theta)$, i.e. the entire magnetosphere is glitched instead of a narrow band. We demonstrate our findings in Fig. 15 where we plot $r\sin(\theta)B_\phi$ at different time-steps

6.3.2 *Narrow symmetric glitch at $\theta = \pi/4$*

The results of the simulation are presented in Fig. 16 (small-scale simulation run,$r_{\rm out} = 10r_\star$), and bottom row of Fig. 17 (long time-scale evolution). In Fig. 16, we show zoomed-in plots for $r\sin(\theta)B_\phi$ superimposed on poloidal field lines for symmetric shear: narrow band near $\theta = \pi/4$ is suddenly moved with angular velocity five times the spin. We start with an unperturbed magnetosphere (Fig. 16a), one period after the star of overall rotation. Then, shear is introduced, Fig. 16(b) – a blue region near the star at $\theta \approx \pi/4$. The resulting shear Alfvén wave breaks out from the magnetosphere, Fig. 16(c). The magnetosphere recovers the bottom row. A new Y-point is formed close to the star (compare locations of the Y-points before the shear is introduced in Fig. 16(a) and right after break-away, Fig. 16d). Outside of the newly formed Y-point reconnection layer forms. It is subjected to plasmoid instability, Figs 16(d)–(e). Eventually, the magnetosphere recovers, to approximately the same location of the Y-point, Fig. 16(f). Notice that the newly formed magnetosphere is twisted: there is non-zero toroidal magnetic field on closed field lines.

6.3.3 *Narrow antisymmetric glitch at $\theta = \pi/2$*

Here antisymmetric shear is needed to produce a CME (otherwise the flux surfaces are just rotated as a whole, see Lyutikov & Sharma 2022). In order to generate antisymmetric, we chose $g(\theta) = \sin^3(\theta)\cos(\theta)$.

As in the previous subsection, we present our results by zooming in close to the star (Fig. 18) and showing the long time-scale evolution (Fig. 19). The results are similar to what we observe for fast symmetric shearing at a band around $\pi/4$: Once the shearing is introduced resulting shear Alfvén wave breaks out, reconnection is observed outside the new Y-point is formed and plasmoid instability is detected, Figs 18(d)–(e). The equilibrium state is shown in Fig. 18(f).

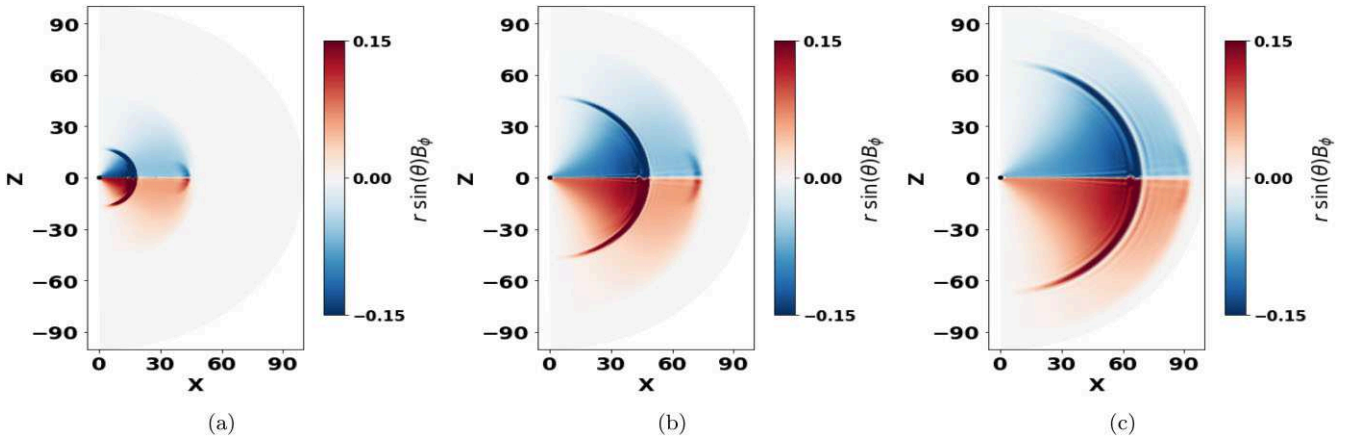

Figure 15. Global glitch with $g(\theta) = const$, large-scale view. Snapshots of $r\sin(\theta)B_\phi$ are taken at $t = 1.6$, 2.5, and 3.2 rotation periods. A glitch produced a global Alfvén wave propagating through the wind.

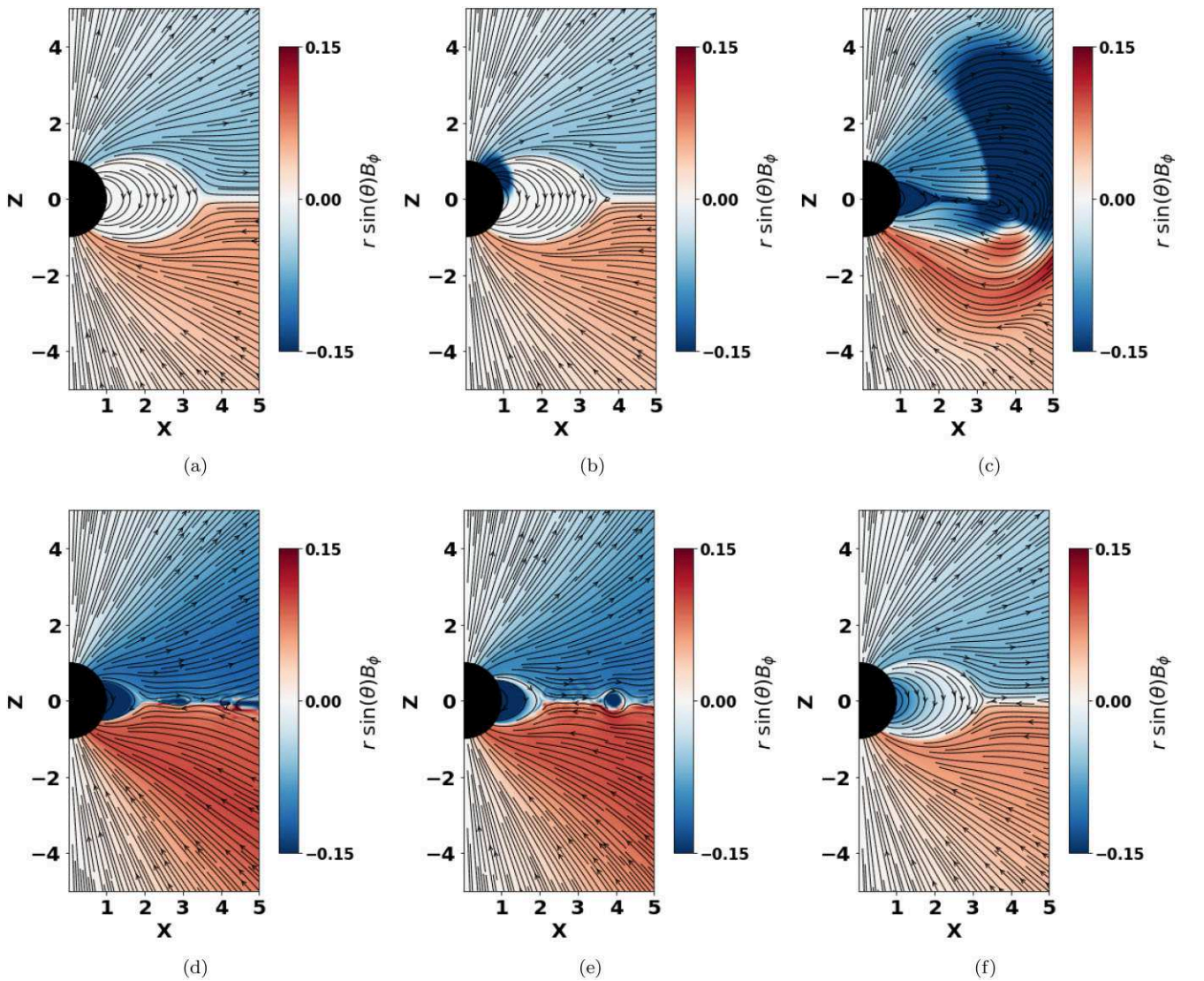

Figure 16. Fast glitch near $\theta = \pi/4$, $g(\theta) = \sin^{10}(\theta + \pi/4)$, dipolar magnetospheres, symmetric shear. The computational domain extends till 10 stellar radius ($r_\star$). Fig. 16(a) is at the time-step just before the glitch is applied whereas Fig. 16(b) is just after. We observe plasmoid island formation in Fig. 16(e). Fig. 16(f) shows the final equilibrium state. See Fig. 17 for similar plots from a large-scale simulation run.

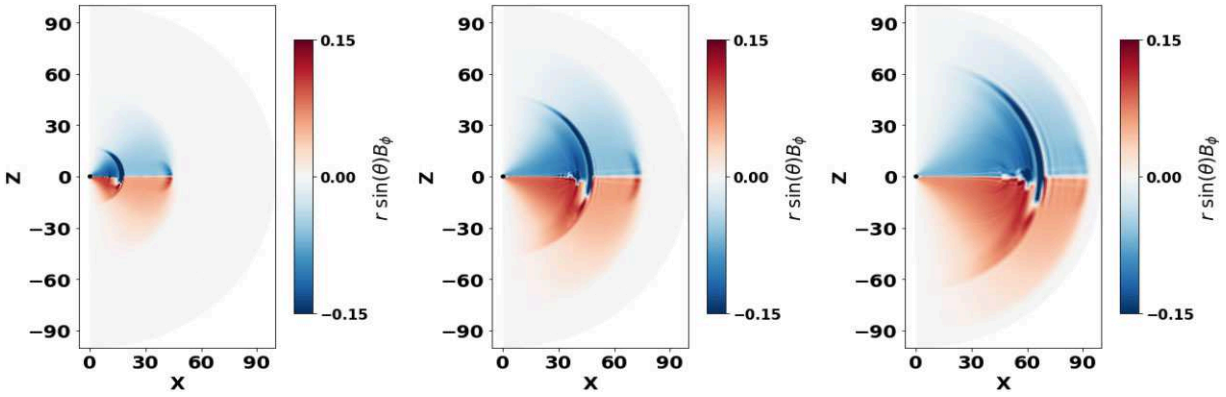

Figure 17. Same as Fig. 16, but for a large-scale run. Snapshots are taken at $t = 1.6$, 2.5, and 3.2. One clearly sees an electromagnetic pulse propagating through the wind.

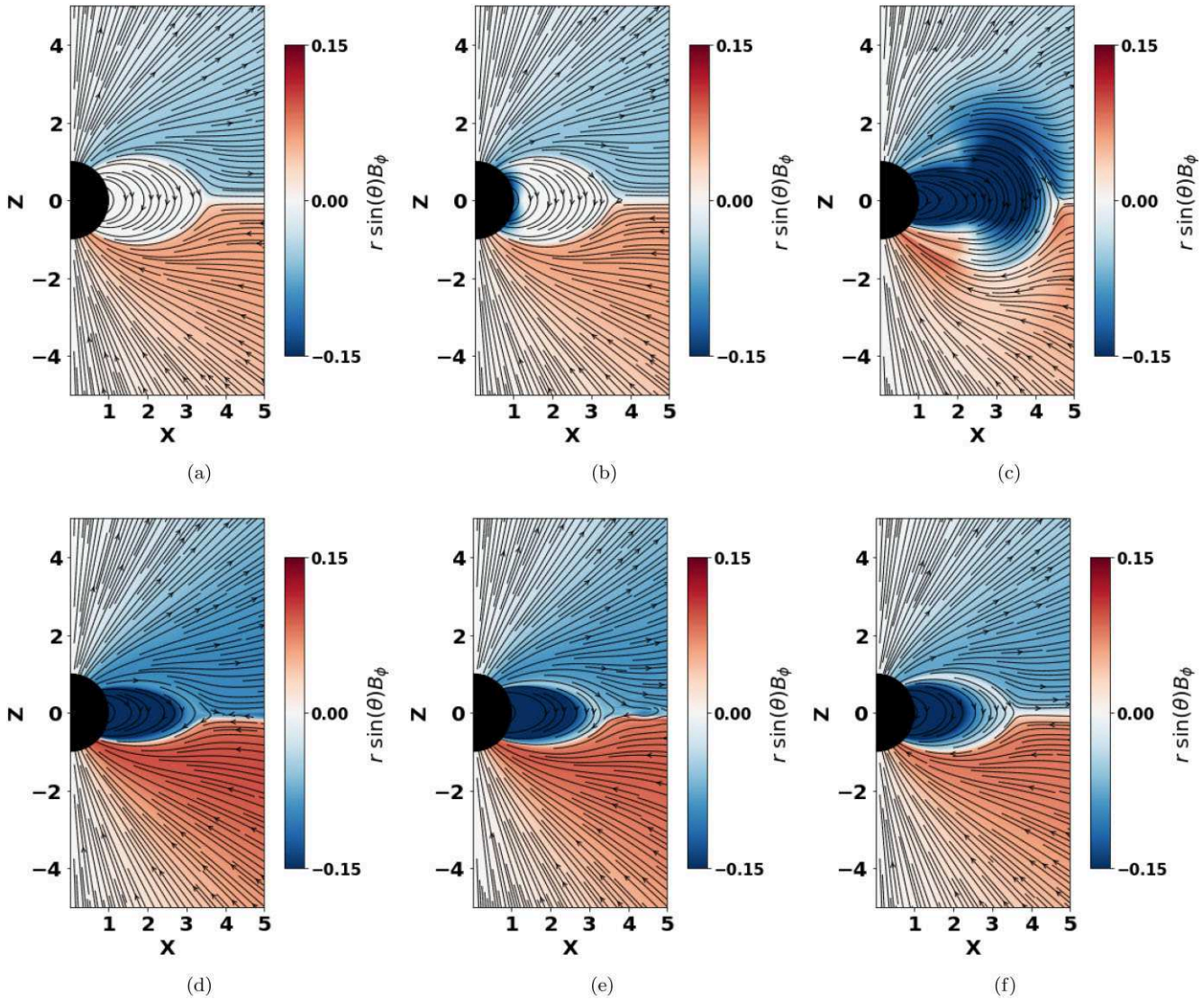

Figure 18. Antisymmetric equatorial glitch with $g(\theta) = \sin^3(\theta)\cos(\theta)$, zoomed-in view. The computational domain extends till 10 stellar radius ($r_\star$). Fig. 18(a) is at the time-step just before the glitch is applied, and Fig. 18(b) is just a one time-step after the initiation of the glitch. Fig. 18(c) shows shearing Alfvén wave breaking away from the magnetosphere. In the lower row, we observe the formation of a new current sheet, subject to plasmoid instability. Fig. 18(f) is the final equilibrium state, with twisted closed field lines.

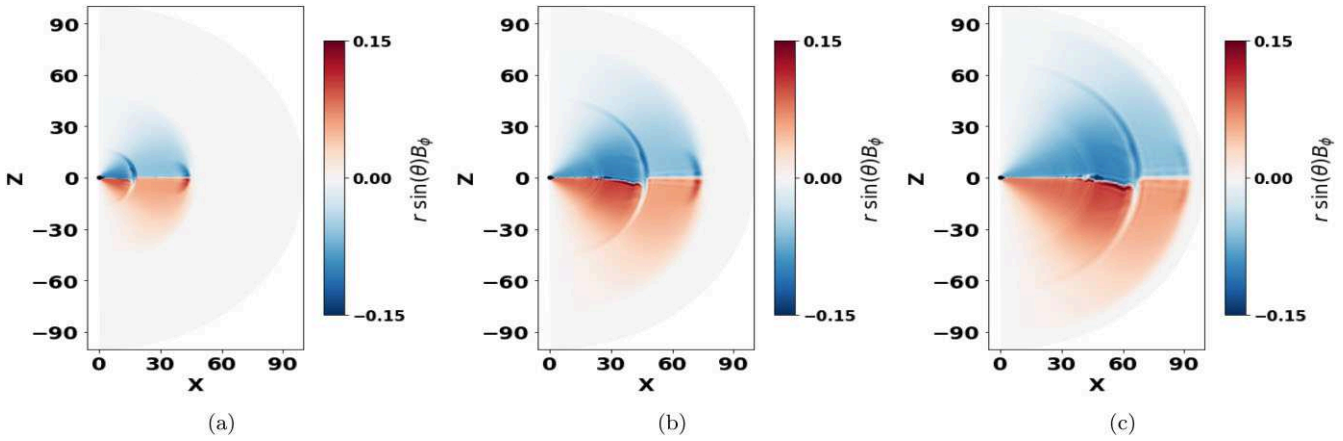

Figure 19. Antisymmetric equatorial glitch, large-scale simulation run at times $t = 1.6$, 2.5, and 3.2.

6.4 Comparison of slow and fast shear, and discussion of previous results

Previously, in Section 5, we considered CME dynamics for slow shear. Let us compare slow and fast shear cases. Concisely: Slow shear generates topologically disconnected CME that is frozen into the wind, while fast shear generates an Alfvén wave propagating through the wind. In both cases, the opening of the magnetosphere is followed by the formation of a reconnection sheet. In the case of slow shear, this opening is achieved by the inflation of the field lines followed by the break-out near the $r_{\rm eq}$ (or near the light cylinder for weaker injections), like in the classical Solar flare models. In the case of fast shear, the opening is achieved by the Alfvén packet itself, exerting a ram pressure on the closed field lines, and breaking them open.

Thus, large amplitude Alfvén waves open up the magnetosphere and form propagating electromagnetic pulses. The magnetosphere recovers by forming a resistive current sheet deep inside the light cylinder, subject to plasmoid instability. Thus, the Alfvén packet in the wind eventually becomes causally disconnected.

Our case of fast shear resembles simulations of Yuan et al. (2020, 2022), who considered the dynamics of shear Alfvén waves within the magnetosphere. In simulation Yuan et al. (2020) an Alfvén wave was added at the initial moment (see our Section 7 for a similar approach). Yuan et al. (2022) do shearing of the foot-points (in 3D). Both simulations of Yuan et al. (2020, 2022) are done close to what we call 'fast shear regime'. In contrast, our 2D simulations allow a slower rate of shear. As we demonstrate, this slow regime leads to qualitatively different dynamics than the fast shear: in the slow case a topologically isolated structure forms, while in the fast regime, electromagnetic waves are launched into the wind. In the slow shear regime, the expanding structure is in an approximate force balance. In the fast shear regime, we demonstrate that the resulting Alfvén pulse within the wind leads to an EM pulse, or even antipulse, not a strong shock wave.

In contrast, we generate the Alfvén wave self-consistently by shearing the foot-points, similar to Parfrey et al. (2013). Our wave amplitude is large: the initial twist is 180°. Thus, the fields in the wave quickly become much larger than the background magnetic field. The Alfvén pulse breaks out from the magnetosphere. During break-out, the pre-explosion closed magnetic field lines are first stretched out, opening the magnetosphere, then reconnection 'behind' the wave pulse sets in. Our 2D fast shear simulations are generally consistent with 3D force-free simulations of Yuan et al. (2022). The similarity includes that the resulting Alfvén pulse opens the magnetosphere.

Recent work by Mahlmann et al. (2023) employs a similar procedure to ours to initialize the explosion – moving of the foot-points; with no light cylinder the corresponding set-up here is like in Section 4. Their 3D calculations naturally are more limited in resolution, especially at large radii. This may be the reason why Mahlmann et al. (2023) did not capture the detonation stage of the expansion.

The opening of the magnetosphere in the fast shear case is somewhat different from the slow shear case. In the case of fast shear, let's assume that the initially generated wave near the neutron star surface has amplitude $\delta B = (\Delta\phi)B_0$, where $(\Delta\phi)$ is a typical angle that the fields lines are sheared. The amplitude of the wave decreases as $\propto R_{\rm NS}/r$ (both Alfvén and X-modes are excited), while the magnetospheric field decreases as $\propto (R_{\rm NS}/r)^3$. The amplitude of the wave becomes larger than the guiding field for

$$\frac{r_{eq,\ EM}}{R_{\rm NS}} \geq (\Delta\phi)^{-1/2}. \tag{26}$$

This is the estimate of the opening scale of the magnetosphere for fast shear, and of the ensuing initial size of the current sheet.

Opening of the magnetosphere requires energy to be spent by the electromagnetic pulse, of the order of

$$B_0^2 \left(\frac{r_{\rm eq,\ EM}}{R_{\rm NS}}\right)^{-6} r_{\rm eq,\ EM}^3. \tag{27}$$

7 LARGE-SCALE DYNAMICS OF INJECTED SHEAR

To complement our analysis of slow and fast shear, we also performed a series of experiments when a packet of shear Alfvén waves is injected into the magnetosphere (instead of the foot point motion). We inject a packet of shear Alfvén waves carrying toroidal magnetic field. In this work, we focus on the scenario where the injection is performed within the magnetosphere. In what follows, we conduct a thorough investigation of the system: How does the location of the ejection influence the dynamics (ejection on open versus closed field lines), and how does the flow react to the value of the injected flux (strong and weak ejections), and how do multiple ejections interact. In what follows, we call the injected Alfvén wave packed as *flux tube*, with a clear understanding that the resulting structure is not

topologically isolated – it is an Alfvén wave packet resembling the flux tube.

7.1 Injection procedure

The setup in this section is as follows. We start with a dipole configuration and let the system evolve unperturbed for two time-periods. We then introduce a flux tube in the magnetosphere of a rotating neutron star in approximate force equilibrium, just slightly out of force balance. We do this by introducing external B_ϕ given by equation (28) for a small but finite time-interval Δt.

The flux tube is taken to be a torus-like structure and embedded in a force-free magnetic environment with the magnetic field along the azimuthal direction. The magnitude of the toroidal field inside the tube is equal to the total poloidal field of a dipole at $r = ar_\star$, where a can be considered as the location of the centre of the flux tube. The flux tube is introduced over a small radial interval at a fixed zenith angle ($\theta_{\rm ft}$)from the z-axis.

In this subsection, since we are interested in tubes inserted inside the light cylinder, we set $a = 2$.

$$B_{\phi,\rm tube} = \sqrt{B_r^2 + B_\theta^2}, \\ = B_0\sqrt{\frac{4\cos[\theta_{ft}]^2}{a^6} + \frac{\sin[\theta_{\rm ft}]^2}{a^6}}. \quad (28)$$

The strength and direction of the toroidal magnetic field inside the tube is controlled by the parameter B_0. For flux inserted along the magnetic wind, B_0 is positive while negative when the tube is inserted against the wind. Thus, the initial configuration is just slightly unbalanced: the dipolar field at the inner edge is somewhat larger than at the outer edge of the flux tube. But as the tube is pushed radially away from the star the flux conservation quickly leads to the creation of a highly overpressurized tube. The tube then both inflates and is pushed out.

The construction of a self-confined flux tube implies that there are surface currents. Surface current K can be calculated via interface conditions of the magnetic field (Jackson 1999).

$$\boldsymbol{K} = \frac{c}{4\pi}[\boldsymbol{n} \times (\boldsymbol{b}_2 - \boldsymbol{B}_1)], \\ \boldsymbol{n} \cdot (\boldsymbol{B}_2 - \boldsymbol{B}_1) = 0. \quad (29)$$

Here, $B_2 = 0$, $B_1 = B_{\phi,\rm tube}$, and n is the unit vector from region 1 (inside the flux tube) to region 2 (outside the tube).

Since the code is sensitive to sudden changes on the magnetic field, the flux tube insertion is inserted over a finite period of time:

$$B_\phi = \begin{cases} B_{\phi,\rm tube}, & \text{if } t_{\rm insertion} \le t \le t_{\rm insertion} + \Delta t \\ 0, & \text{otherwise}. \end{cases} \quad (30)$$

One important quantity is the toroidal flux added within the flux tube.

$$\Phi = \int_{S_t} \vec{B} \cdot \vec{n} {\rm d}S. \quad (31)$$

In the case of magnetar-generated CME, the magnetic flux carried by the flux tube originating near the surface can be estimated as

$$\Phi_{\rm f} \sim B_\star R_{\rm f}^2 = B_\star \eta_{\rm f}^2 R_\star^2, \quad (32)$$

where $R_{\rm f}$ is a typical size of the active region and in the latter equality we scaled flare's size to the radius of the neutron star, $R_{\rm f} = \eta_{\rm f} R_\star$,

The value of the added toroidal flux can be compared with the total toroidal flux within the light cylinder (in one hemisphere) generated by the rotating dipole. The model of Goldreich & Julian (1969) gives

Table 4. Table showing toroidal flux injected to the system $\Delta\Phi$ for different values of Δt.

Δt	$\Phi_{\rm i}$	$\Phi_{\rm f}$	$\Delta\Phi$	$\lvert\frac{\Delta\Phi}{\Phi_{\rm i}}\rvert$
0.03	−0.24	−0.54	−0.30	1.25
0.06	−0.24	−0.85	−0.61	2.5
0.16	−0.24	−1.43	−1.19	4.9

an estimate

$$\Phi_i \sim B_\star R_\star^2 \left(\frac{\Omega_\star R_\star}{c}\right). \quad (33)$$

The injected magnetic flux therefore can be calculated via,

$$\Delta\Phi = \Phi_f - \Phi_i, \quad (34)$$

where $\Phi_{\rm f}$ is the toroidal flux at $t = t_f = t_{\rm insertion} + \Delta t$ and $\Phi_{\rm i}$ is the flux at $t = t_i = t_{\rm insertion}$. Here, $t_{\rm insertion}$ is the simulation time-step at which the flux tube was introduced in the system for a duration of Δt. In this work, we display our results for $t_{\rm insertion} = 2$ and $\Delta t = 0.06$, with time expressed in terms of the unperturbed rotational period of the star.

For $\Delta\Phi \sim \Phi_{\rm f}$, we expect

$$\lvert\frac{\Delta\Phi}{\Phi_i}\rvert \sim \eta_f^2 \frac{c}{\Omega_\star R_\star} \ge 1. \quad (35)$$

Thus, the toroidal magnetic flux injected by the flare is expected to be of the order of the total toroidal magnetic flux of unperturbed magnetosphere. Our simulations' parameters, Table 4, use similar values.

7.2 Dynamics of shear Alfvén waves in the magnetosphere and the preceding wind

For our first sets of experiments, we add a single toroidal flux tube following the procedure described in Section 7.1. The tube is launched at $a = 2$ (we remind that for our basic set-up, the light cylinder is at $x = 5$). We explored two injection sites: at $\theta_{\rm injection} = 60^\circ$ (so that the injection is on closed field lines) and at $\theta_{\rm injection} = 30^\circ$ (so that the injection is on open field lines). We also explored two polarizations of the injected waves which we call symmetric (so that the toroidal field in the wave is of the same sign as the toroidal field in the corresponding hemisphere of the wind), and antisymmetric (so that the toroidal field in the wave is of the same sign as the toroidal field in the corresponding hemisphere of the wind).

Though the waves are injected with similar procedures, the addition of the toroidal component, in fact, corresponds to somewhat different modes. On the open field lines, there is already B_ϕ present. This toroidal field determines the spin-down: the addition of an extra toroidal field modifies the spin-down, see Sections 6 and 7.3. The addition of the toroidal component on the close field lines generates both Alfvén waves (propagating mostly along the magnetic field), and compressional X-mode (propagating approximately radially).

While the Alfvén components of the resulting pulse add differently to the wind flow (depending on the strength and polarization), see Fig. 20, the X-mode component always produces a compression: a forward propagating wave, Fig. 21.

Our basic results are plotted in Fig. 20 for injection on closed field lines ('symmetric' injection). We observe that the injected flux tube first expands within the magnetosphere (top two left-hand panels) and then propagates as an Alfvén pulse in the wind.

To further elucidate the underlying dynamics in Fig. 21, we compare later behaviour for 'antisymmetric' injection at two locations:

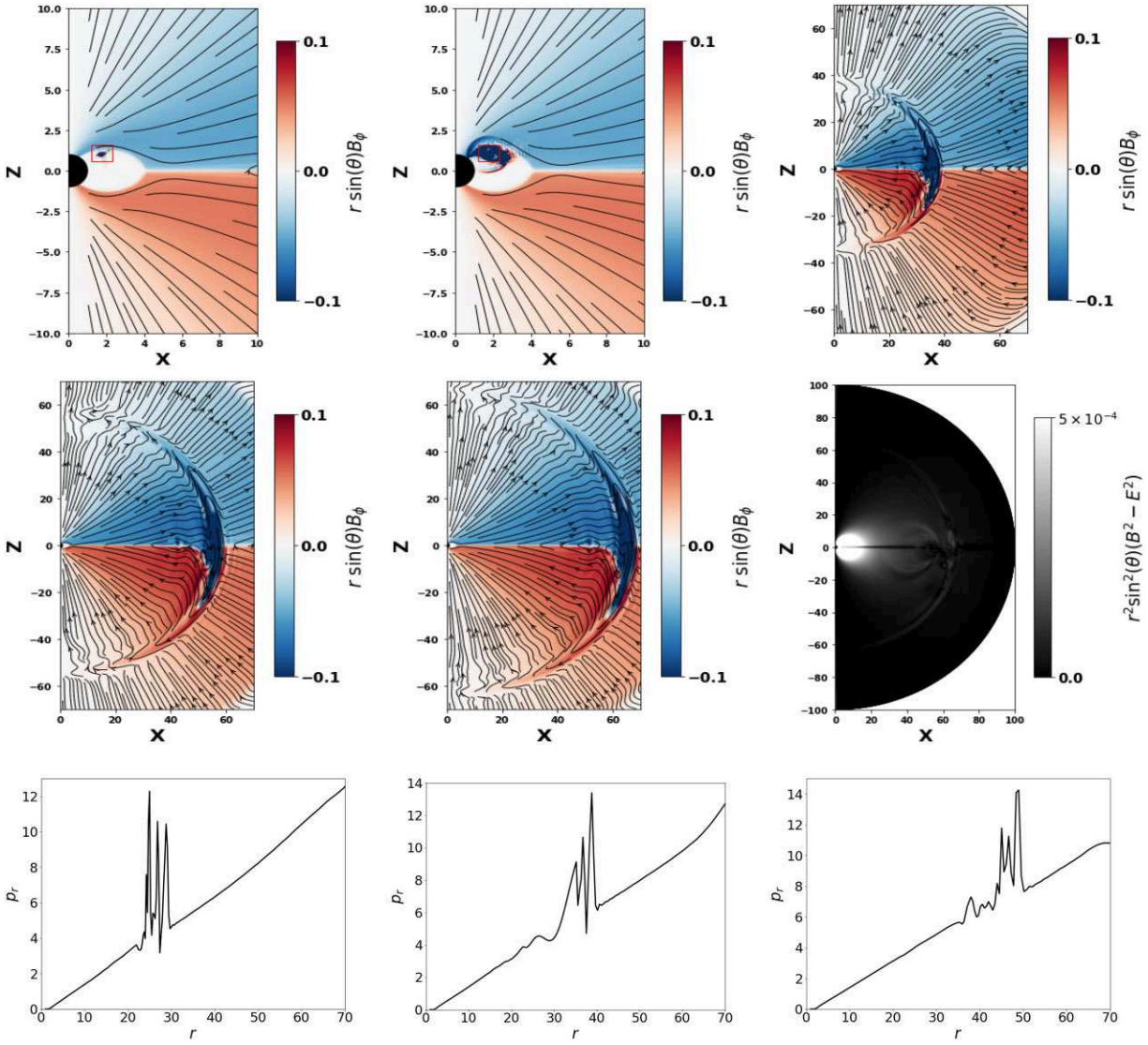

Figure 20. Flux tube/Alfvén wave packet launched on closed field lines at 60° from zenith and radial distance $a = 2$, 'symmetric' injection, at times $t = 2.01$, 2.04, 3.2, 3.8, and 4.1 (launching at $t = 2$, $\Delta t = 0.06$). The left and middle figures, in the top panel, show the zoomed-in version to capture the flux tube just after the launch. In the first plot, the injected flux tube is a small patch, highlighted within a rectangle for visual clarity. We observe that the flux tube expands quickly within the light cylinder. The right greyscale figure, in the middle panel, shows the absolute value of effective magnetic field $(B^2 - E^2) \times r^2 \sin^2\theta$ at $t = 4.1$; it demonstrates that with the flux tube Alfvén pulse, there are no large variations of the effective magnetic field. The bottom panel shows the magnitude of radial momentum p_r as a function of radial distance r for a slice at 60° from the pole at $t = \{2.9, 3.2, 3.5\}$. A forward-propagating pulse is clearly seen. We also repeated the calculations for an angular slice at 120° and the results were similar.

$\theta = 30°$ (left-hand panel) and $\theta = 60°$ (right-hand panel). In both cases, the injection is 'weak' – meaning that the injected toroidal flux is somewhat smaller than (33). The two cases are clearly different: for 'antisymmetric' injection on open field lines *a backward propagating wave is launched* (in panel 21, the radial momentum within the wave is *smaller* than that of the wind.)

At the same time, the similar injection but on closed field lines (right-hand panels in Fig. 21) creates *forward* propagating pulse. The reason for the differences is the following. For 'antisymmetric' injection on open field lines, the resulting Alfvén pulse resembles the magnetospheric glitch, Section 6 – regions with smaller toroidal fields propagate slower. We also verified that in the case of a 'strong antisymmetric' injection, when the injected toroidal flux is larger than (33), the resulting pulse is forward-propagating.

Qualitatively, using Michel's solution (22) a local toroidal magnetic field corresponds to some local effective angular velocity. Reducing local toroidal magnetic field (for weak antisymmetric injection) reduces the effective angular velocity and the radial momentum. Since the radial momentum p_r is a quadratic function of the field, strong antisymmetric injection (so that the total toroidal field is larger inside the pulse than in the surrounding wind) produces a forward propagating pulse.

Injection on the closed field lines proceeds differently. For 'mild' injection, the added toroidal field on the closed field lines corresponds to fast mode regardless of the polarization. The fast mode first propagates through the magnetosphere and then creates *compression* of the field in the wind. The resulting pulse is always forward propagating.

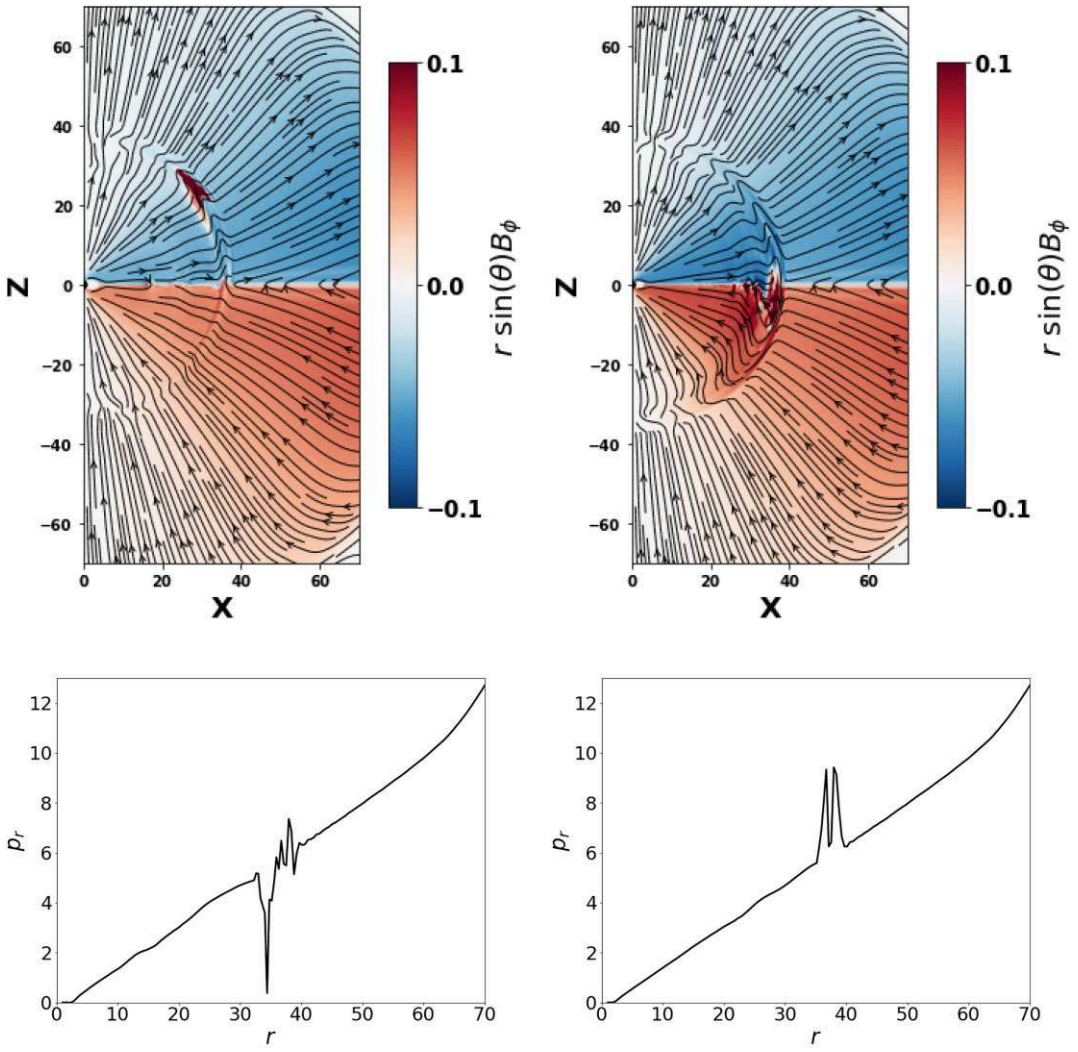

Figure 21. Comparison of injections on open field lines $\theta = 30^\circ$ (left-hand column) and closed field $\theta = 60^\circ$ (right-hand column). Weak 'antisymmetric' injection. Notice that injection on open field lines produces a pulse that is backward propagating through the wind. For injection on closed field lines, the fast mode propagating with the magnetosphere creates an electromagnetic pulse that propagates in a forward direction through the wind independently on the initial polarization of the pulse.

7.3 Multiple injection events

We end this section by considering the scenario of multiple flux tubes. Here, we add two flux tubes, the first one at $t = t_{\rm insertion}$, and the second one at $t = 1.5t_{\rm insertion}$ with time expressed in terms of the rotational period of the star. The first tube is weaker and launched against the wind (antisymmetric scenario) while the second tube is stronger and launched along the wind. We consider injections on open field lines $\theta = 30^\circ$ and closed field $\theta = 60^\circ$. We show a snapshot of such a multiflux tube system in Figs 22(a) and (b) The two tubes do not catch up, even if the second one is more powerful and the first is 'weak-antisymmetric' launched on open field lines (hence propagating backward through the wind).

This is clearly a result of relativistic kinematics, modified by the fact that the bulk flow is accelerating. In fact, Alfvén waves propagating in Michel's wind can be considered non-perturbatively, Lyutikov (2011) and Section 6. Such waves can be parametrized by the local spin $\Omega_{1,2} \neq \Omega_0$ (Ω_0 is the constant spin of the star). One then finds the location of the first wave at time t after leaving the light cylinder:

$$R_1 = \frac{1}{2}\left(t + \frac{1}{\Omega_0} - \frac{\Omega_0}{\Omega_1^2}\right) + \sqrt{1 + \frac{\left(\Omega_1^2(1 + t\Omega_0) - \Omega_0^2\right)^2}{4\Omega_0^2\Omega_1^2}}\frac{1}{\Omega_1} \approx t + \frac{1}{\Omega_0} - \frac{\Omega_0}{\Omega_1^2} + \frac{1}{t\Omega_1^2}, \tag{36}$$

where $R_0 = 1/\Omega_0$ (wave is launched at time $t = 0$ at the light cylinder); the latter relation is for $t \gg 1/\Omega_0$. Equation (36) gives the location of the Alfvén pulse propagating through accelerating wind.

If a second Alfvén pulse is launched after time Δt with $\Omega_2 \geq \Omega_1$, the collision will occur approximately at

$$t_{coll}\Omega_0 \approx \left(1 + \frac{\Delta t\Omega_1^2\Omega_2^2}{\Omega_0\left(\Omega_1^2 - \Omega_2^2\right)}\right)^{-1} \approx \frac{1}{2}\Omega_0^2\left(\frac{1}{\Omega_1^2} - \frac{1}{\Omega_2^2}\right), \tag{37}$$

where the last relation assumes that the two pulses are separated by one rotation. Typical collision times are long and not captured by our simulations. When the waves eventually catch up at $r \gg R_{\rm LC}$,

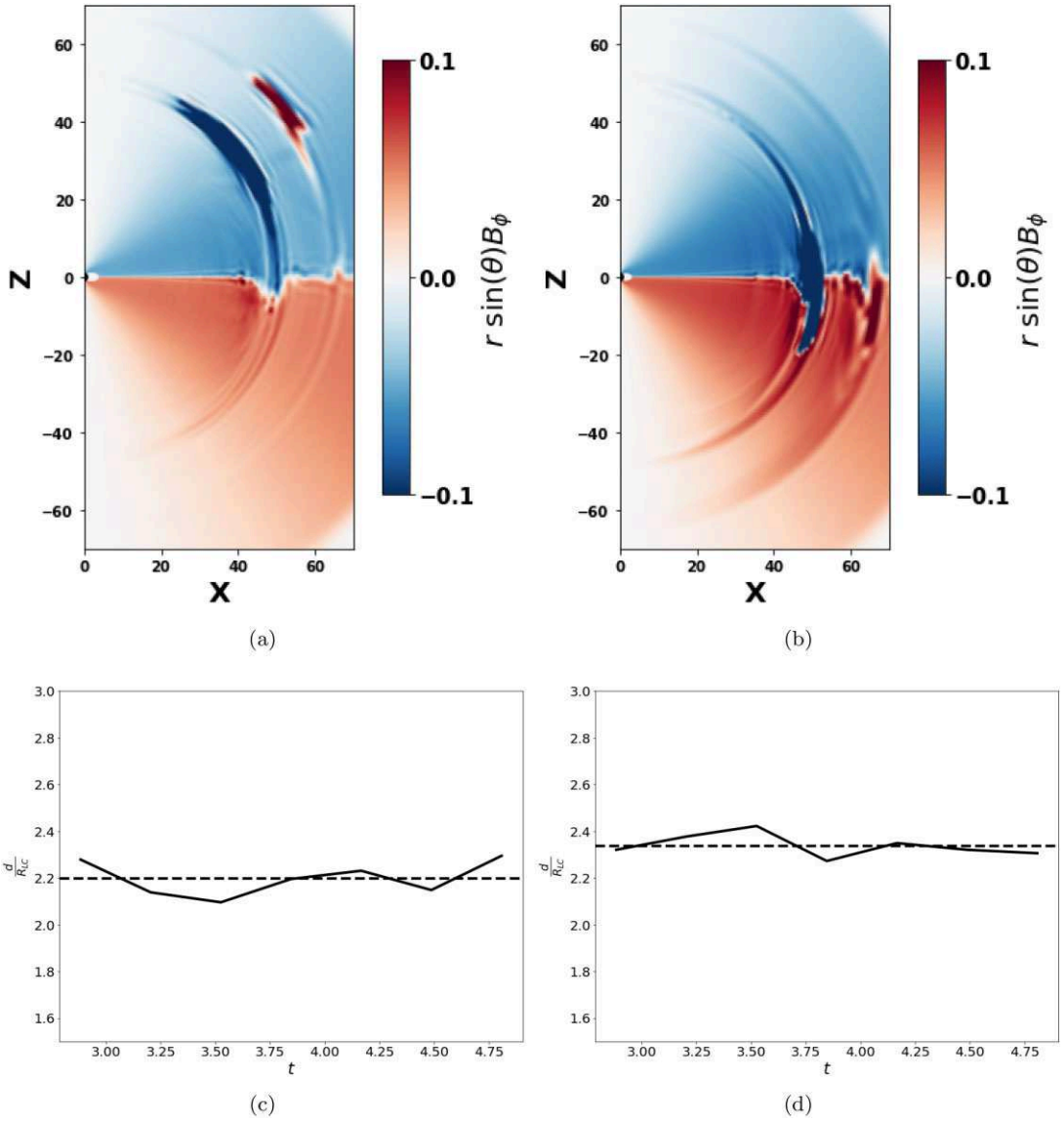

Figure 22. Multiple injection events. Two tubes are injected inside the light cylinder at spherical radius $a = 2$. Injection occurs at 30° (left-hand column, on open field lines) and 60° (right-hand column, on closed field lines). The first tube is *weak-antisymmetric*, and the second tube was launched half rotational period after the first one. Bottom row: time evolution of the distance between the two flux tubes (normalized with respect to the radius of the light cylinder). The solid line represents the separation between the tubes as a function of time, whereas the dashed line shows the average separation. As observed, the separation between the injections remains (approximately) the same.

the interaction will resemble the interaction between two non-linear packets of fast modes.

8 CONCLUSION: WHENCE TO FRB

In this work we continue, following Lyutikov (2022), Barkov et al. (2022), and exploration of the dynamics of the relativistic magnetized explosions: How relativistic magnetically driven explosions are produced by magnetars, and how they propagate through the preexisting magnetized wind. To search for answers, we performed multiple 2D numerical simulations of a neutron star magnetosphere and the winds. The simulations focused on several different but related phenomenons: production of magnetic flares via shearing of the foot-points of the magnetic field lines, and evolution of relativistic flux tube(s)/Alfvén pulses in magnetars' winds.

Two regimes of foot-points shearing, we considered (i) slow shear so that the whole inflated magnetic arc structure is in a state of causal contact; (ii) fast shear so that the corresponding dynamics resemble large amplitude Alfvén waves injected into the magnetosphere.

We stress again the importance of magnetic loading of magnetar flares (Barkov et al. 2022; Lyutikov 2022): an injected flux tube/plasmoid loses a lot of energy trying to break out from the magnetosphere. For example, we expect that a fraction of the injected magnetic energy $E_{\rm CME,\,0}$ will be emitted in X-rays. Yet the energy that gets deposited into the wind even in the supercritical case is always much smaller at least by the small numerical factor η_E (the ratio of injected energy to the total magnetospheric energy); for the flux tube scenario, the decrease is even more dramatic, $\propto \eta_{\rm e}^2$, see Table 1. For milder flares, the wind adjusts to the perturbation right near the light cylinder, so no energy is deposited in the wind.

Though force-free simulations naturally do not allow shock formations, in the 'magnetic bomb' paper Barkov et al. (2022) both MHD and force-free simulations were done, showing that there is a clear regime – detonation. Briefly, the dynamics of a flux tube or a CME within the magnetosphere are controlled by two factors: conservation of the magnetic flux and work done on the opening of the overlaying magnetic field lines. The energy contained within the CME decreases as $\propto 1/r$. The energy of the dipolar field external to the CME decreases as $\propto 1/r^4$. As a result, at some radius $r_{\rm eq}$ the energy of the CME is larger than the energy of the confining field. At radii smaller than $r_{\rm eq}$, the structure is volume-filled. After detonation, the magnetic field is concentrated near the surface of the expanding structure. The ensuing expansion of a CME (modelled as a spheromak) becomes supersonic. In the force-free case, we see the spheromak torn apart and also become causally disconnected. This is detonation. After detonation, the CME stops losing energy on the external matter/field and will form a weak shock-like event in the magnetar wind. In application here, with force-free simulations only, we argue that before the detonation happens (if at all) an expending structure already loses a lot of energy. So, simple estimates that an injection of energy E_0 will somehow affect the wind, are off by orders of magnitude. For subcritical injections, when the energy of the CME is small and $r_{\rm eq}$ is beyond the light cylinder, so that there is no detonation inside the, the resulting CME is a structure in force balance, and advected passively with the wind. If the CME's energy exceeds the critical and detonation occurs, then still only a small fraction of the initial energy, at most $\sim\eta_E$, is transferred to the wind in the form of an EM pulse.

We conclude that:

(i) For slow shear, the *Solar flare* paradigm:

(a) There are two possible stages of CME expansion within the magnetosphere: for sufficiently large injection, a CME experiences internal detonation at some radius $r_{\rm eq}$, when it starts expanding relativistically within the magnetosphere and loses causal connection.

(b) The magnetospheric dynamics depends both on the large-scale structure and on the location of shearing foot points: to generate rare powerful events shear must occur on field lines that 'close-in' near the star; otherwise, numerous weak events are generated.

(c) Ejected magnetic blobs, CMEs, are frozen into the wind

(ii) For fast shear, the *Star quake* paradigm:

(a) Shearing of foot-points leads to the generation of Alfvén wave; the pressure of the Alfvén leads to opening of the magnetosphere (no wave breaking).

(b) Resulting perturbations propagate in the wind as shear Alfvén waves, with no breaking

(c) Multiple shear Alfvén waves are unlikely to collide within relativistically accelerating wind.

(iii) In both cases of slow and fast shear, no considerable dissipation occurs in the wind zone. In both cases after the ejection, the magnetosphere first opens; afterward, the newly closed magnetosphere is smaller, and recovers resistively.

Our results are complementary to those of Barkov et al. (2022), who investigated the dynamics of magnetic explosions with complicated, linked magnetic internal stricture. Computations presented by Barkov et al. (2022) describe the case when a CME expands beyond the light cylinder. In that case, the initial dynamics, both in highly magnetized MHD and force-free cases, were similar to what we observed: an overpressurized magnetic structure first rapidly expanded. The long-term dynamics had two possibilities depending on the initial energy and the structure of the wind: a magnetic bubble either expands nearly self-similarly with the wind (for weaker explosions) or detonates – creating internally causally disconnected structures.

Our results make a consistent picture: powerful strongly magnetized ejected blobs/flux tube makes minimal distortion in the wind. They either quickly reach force-balance with the wind, and propagate self-similarly, without producing shocks and/or dissipative structures, or propagate as highly weakened electromagnetic disturbances. This picture is in sharp contrast with the hydrodynamics, where overpressurized regions create a strong dissipative shock.

Our results have implications for the generation of FRBs.

(i) *FRBs as CMEs – large and small*. FRBs show a large range of luminosities (CHIME/FRB Collaboration 2020; Shin et al. 2023), which raises an obvious question: what's the control parameter that defines (both X-ray and radio) luminosity of magnetars' bursts/flares? The overall size involved in a flare is one obvious parameter. Another is the strength of the magnetic field – both determine total energetics.

In the Solar flare paradigm of magnetar flares, the magnetic field also enters via the rate of shearing the foot-point: the shearing rate is $\propto$ magnetic field (Goldreich & Reisenegger 1992); thus, qualitatively, the magnetar activity is a B^3 function of the magnetic field (Lyutikov 2015).

In this work, we find that other, less clearly measured properties play a role: (i) evolution of a CME within magnetosphere proceeds in different regimes depending on the injected energy (possibly a detonation); (ii) location of the shear; (iii) overall structure of the magnetosphere. If shearing is done near the fields that extend far out from the star, then the twist is easily released in many small flares. (Along a given field line, the twist concentrates near the regions of weakest magnetic field, hence at the highest point in the magnetosphere.) In order to produce rare and powerful explosions, the shearing should be done at the foot-points of field lines that close in, roughly speaking, within a stellar radius.

Qualitatively, a twist of a given magnetic field line concentrates near the points where the guiding field is the weakest – at the furthest extent. It is there that the stability is determined. For field lines extending to large distances, the guiding field is small, so that the kink instability is easily initiated at small twists. The system then gets rid of the twist in many small events.

Finally, the presence of the light cylinder effectively impedes the storage of the magnetic energy. If an inflated flux tube reaches the light cylinder before reaching the detonation stage, $R_{\rm LC} \leq r_{\rm eq}$, it opens up and releases the twist which limits the amount of magnetic energy that can be stored. Thus, to produce strong flares the spin period *should not* be too short.

(ii) *Dynamics of CMEs/electromagnetic pulses in the preceding wind*. Our results on the wind dynamics are in some contradiction to the 'wind models' of FRBs (e.g. Lyubarsky 2014; Beloborodov 2017; Metzger et al. 2019; Thompson 2023). For slow shear, the Solar flare paradigm, energetically mild CME (non-detonating) produces a minimal distortion of the wind: topologically disconnected structures ('magnetic shells') come into force balance close to the light cylinder, and are then passively advected with the flow. In the supercritical detonating case, a highly weakened electromagnetic pulse is launched into the wind. For fast shear, the Starquake paradigm, the energy is quickly deposited into the magnetosphere in the form of Alfvén and X-modes that may also open the magnetosphere. In doing so, the

wave energy is deposited into the magnetosphere, so is lost by the pulse.

In passing, we note that the original shock model of Gallant et al. (1992), Hoshino et al. (1992), envisioned to explain *months-long* variability of Crab Nebula wisps, involves the interaction of the relativistic wind with heavy ejecta. In that case, the cyclotron instability occurs in the termination shock of the wind, with only mildly relativistic post-shock flow. It does not apply to the generation of millisecond (and even shorter) radio pulses in FRBs.

ACKNOWLEDGEMENTS

This work had been supported by NASA grants 80NSSC17K0757 and 80NSSC20K0910, NSF grants 1903332 and 1908590. We would like to thank Spiro Antiochos, Jens Mahlmann, and Chris Thomson for their comments and discussions. The work of the organizers of the 'Plenty of Room at the Bottom: Fast Radio Bursts in our Backyard' workshop is acknowledged.

DATA AVAILABILITY

The data underlying this article will be shared on reasonable request to the corresponding author.

REFERENCES

Abramowitz M., Stegun I. A., 1972, Handbook of Mathematical Functions. National Bureau of Standards, Maryland
Aly J. J., 1980, A&A, 86, 192
Aly J. J., 1991, ApJ, 375, L61
Antiochos S. K., DeVore C. R., Klimchuk J. A., 1999, ApJ, 510, 485
Antiochos S. K., DeVore C. R., Karpen J. T., Mikić Z., 2007, ApJ, 671, 936
Barkov M. V., Komissarov S. S., 2016, MNRAS, 458, 1939
Barkov M. V., Popov S. B., 2022, MNRAS, 515, 4217
Barkov M. V., Sharma P., Gourgouliatos K. N., Lyutikov M., 2022, ApJ, 934, 140
Beloborodov A. M., 2017, ApJ, 843, L26
Bochenek C. D., Ravi V., Belov K. V., Hallinan G., Kocz J., Kulkarni S. R., McKenna D. L., 2020, Nature, 587, 59
Bogovalov S. V., 1999, A&A, 349, 1017
Brennan T. D., Gralla S. E., Jacobson T., 2013, Class. Quant. Grav., 30, 195012
CHIME/FRB Collaboration, 2020, Nature, 587, 54
CHIME/FRB Collaboration, 2022, Nature, 607, 256
Contopoulos I., Kazanas D., Fendt C., 1999, ApJ, 511, 351
Cordes J. M., Chatterjee S., 2019, ARA&A, 57, 417
Del Zanna L., Papini E., Landi S., Bugli M., Bucciantini N., 2016, MNRAS, 460, 3753
Forbes T. G., 2000, J. Geophys. Res., 105, 23153
Gallant Y. A., Hoshino M., Langdon A. B., Arons J., Max C. E., 1992, ApJ, 391, 73
Goldreich P., Julian W. H., 1969, ApJ, 157, 869
Goldreich P., Reisenegger A., 1992, ApJ, 395, 250
Gourgouliatos K. N., Cumming A., Reisenegger A., Armaza C., Lyutikov M., Valdivia J. A., 2013, MNRAS, 434, 2480
Gralla S. E., Jacobson T., 2014, MNRAS, 445, 2500
Hoshino M., Arons J., Gallant Y. A., Langdon A. B., 1992, ApJ, 390, 454
Hurley K. et al., 2005, Nature, 434, 1098
Jackson J. D., 1999, Classical Electrodynamics, 3rd edn. Wiley, New York, NY
Kaspi V. M., Beloborodov A. M., 2017, ARA&A, 55, 261
Khangulyan D., Barkov M. V., Popov S. B., 2022, ApJ, 927, 2
Komissarov S. S., 2006, MNRAS, 367, 19
Komissarov S. S., Barkov M. V., 2007, MNRAS, 382, 1029
Komissarov S. S., Barkov M., Lyutikov M., 2007, MNRAS, 374, 415
Levin Y., Lyutikov M., 2012, MNRAS, 427, 1574
Li Y., Luhmann J. G., 2005, AGU Spring Meeting Abstracts. American Geophysical Union, Washington, D.C., p. SH51C–08
Lyubarsky Y., 2014, MNRAS, 442, L9
Lyutikov M., 2003, MNRAS, 346, 540
Lyutikov M., 2006, MNRAS, 367, 1594
Lyutikov M., 2010, Phys. Rev. E, 82, 056305
Lyutikov M., 2011, Phys. Rev. D, 83, 124035
Lyutikov M., 2013, preprint (arXiv:1306.2264)
Lyutikov M., 2015, MNRAS, 447, 1407
Lyutikov M., 2021, ApJ, 922, 166
Lyutikov M., 2022, MNRAS, 509, 2689
Lyutikov M., 2023, MNRAS, 520, 4315
Lyutikov M., Hadden S., 2012, Phys. Rev. E, 85, 026401
Lyutikov M., McKinney J. C., 2011, Phys. Rev. D, 84, 084019
Lyutikov M., Popov S., 2020, preprint (arXiv:2005.05093)
Lyutikov M., Sharma P., 2022, MNRAS, 513, 1947
Lyutikov M., Burzawa L., Popov S. B., 2016, MNRAS, 462, 941
Mahlmann J. F., Philippov A. A., Mewes V., Ripperda B., Most E. R., Sironi L., 2023, ApJ, 947, L34
Mereghetti S., 2008, A&A Rev., 15, 225
Mereghetti S. et al., 2020, ApJ, 898, L29
Metzger B. D., Margalit B., Sironi L., 2019, MNRAS, 485, 4091
Michel F. C., 1973, ApJ, 180, L133
Mikic Z., Linker J. A., 1994, ApJ, 430, 898
Palmer D. M. et al., 2005, Nature, 434, 1107
Parfrey K., Beloborodov A. M., Hui L., 2012, MNRAS, 423, 1416
Parfrey K., Beloborodov A. M., Hui L., 2013, ApJ, 774, 92
Parfrey K., Spitkovsky A., Beloborodov A. M., 2017, MNRAS, 469, 3656
Petroff E., Hessels J. W. T., Lorimer D. R., 2019, A&A Rev., 27, 4
Popov S. B., Postnov K. A., 2013, preprint (arXiv:1307.4924)
Ridnaia A. et al., 2021, Nat. Astron., 5, 372
Ripperda B., Porth O., Sironi L., Keppens R., 2019, MNRAS, 485, 299
Shin K. et al., 2023, ApJ, 944, 105
Thompson C., 2023, MNRAS, 519, 497
Thompson C., Duncan R. C., 1995, MNRAS, 275, 255
Thompson C., Duncan R. C., 2001, ApJ, 561, 980
Usov V. V., 1992, Nature, 357, 472
Vourlidas A., Buzasi D., Howard R., Esfandiari E., 2002, J. Kuijpers. ESA, Noordwijk, p. 91
Wolfson R., Low B. C., 1992, ApJ, 391, 353
Wood T. S., Hollerbach R., Lyutikov M., 2014, Phys. Plasmas, 21, 052110
Younes G. et al., 2023, Nat. Astron., 7, 339
Yuan Y., Beloborodov A. M., Chen A. Y., Levin Y., 2020, ApJ, 900, L21
Yuan Y., Beloborodov A. M., Chen A. Y., Levin Y., Most E. R., Philippov A. A., 2022, ApJ, 933, 174

APPENDIX A: DIPOLE-PLUS-QUADRUPOLE CONFIGURATIONS

In this case, fairly simple analytical results can guide us in the choice of shearing location. The flux function for dipole and quadrupole, normalized to magnetic field at the pole is

$$P_{\rm d} = \frac{\sin^2\theta}{r}\frac{B_{\rm p}R^3}{2}$$
$$P_{\rm q} = \frac{\sin(2\theta)\sin\theta}{r^2}\frac{B_{\rm q}R^4}{4}$$
$$\boldsymbol{B}_{\rm d,q} = \nabla P_{\rm d,q}\times\nabla\phi. \quad \text{(A1)}$$

The total field is a linear sum

$$P_{\rm tot} = P_{\rm d} + \mu_{\rm q}P_{\rm q}, \quad \text{(A2)}$$

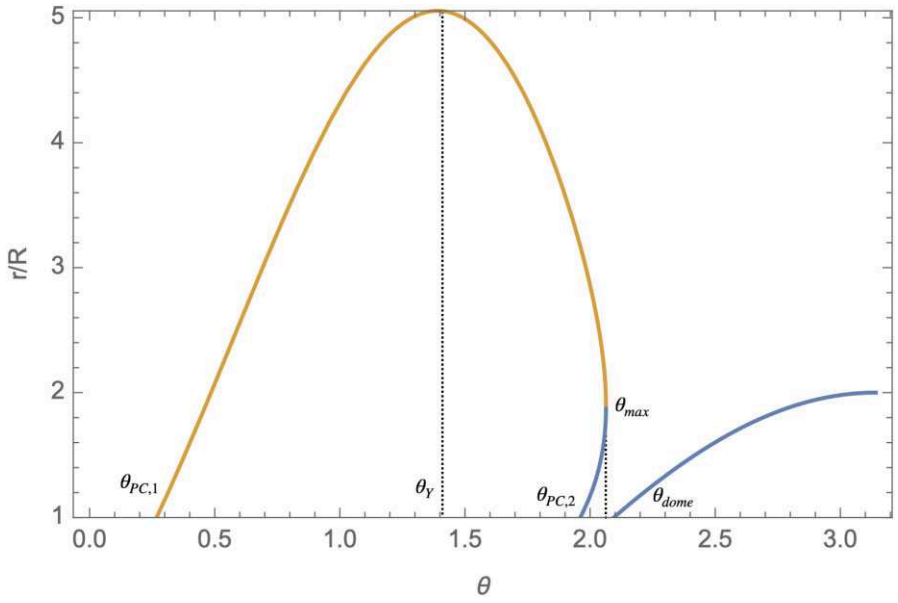

Figure A1. Last closed field lines and the southern dome for the dipole-plus-quadrupole configuration with $\mu_q = 2$.

where μ_q parametrizes the relative strength of the dipole and quadrupole. We use $\mu_q = 2$: This makes the magnetic field at one pole three times larger than pure dipole, while at the other pole magnetic field equal in value to the dipole value, but with the reverse sign.

We find special points:

(i) Zero point at antipole corresponds to $\mu_q = 1$.

(ii) Edge of the southern dome $\cos\theta_{\rm dome} = -1/\eta$ ($\theta_{\rm dome} = 2\pi/3$ for $\mu_q = 2$).

(iii) Upper polar cap. Furthest point at $R_{\rm LC} = r\sin\theta_Y$, ($\theta_Y$ is the angle of the Y-point

$$\eta = -\frac{6\cot(\theta_Y)}{5\cos(2\theta_Y)+3}\frac{R_{\rm LC}}{R}. \tag{A3}$$

For $R_{\rm LC}/R = 5$ and $\eta = 2$, $\theta_Y = 1.4480$ (θ_Y cannot be smaller than $\cos(2\theta_Y) = -3/5$). Y-point is at $r = R_{\rm LC}/\sin\theta_Y \to 5.037$.

(iv) At the last open field line

$$P_{\rm tot}^{(0)} = \frac{\sin^3(\theta_Y)\cos(2\theta_Y)}{5\cos(2\theta_Y)+3}\frac{1}{R_{\rm LC}}. \tag{A4}$$

The last closed field lines are given by

$$r^{(0)} = \frac{\sin^2(\theta) \pm \sin(\theta)\sqrt{\sin^2(\theta) + 8\eta P_{\rm tot}^{(0)}\cos(\theta)}}{4P_{\rm tot}^{(0)}}. \tag{A5}$$

The maximal extent is when they are equal,

$$\cos\theta_{\rm max} = 4P_{\rm tot}^{(0)}\mu_q - \sqrt{1+(4P_{\rm tot}^{(0)}\eta)^2}. \tag{A6}$$

Polar cap polar angles are as follows:

$$\theta_{\rm PC,1} = 0.267,$$
$$\theta_{\rm PC,2} = 1.96. \tag{A7}$$

APPENDIX B: ROTATING STARS WITH NO FOOT-POINT SHEARING

As a preliminary investigation, we considered rotating but unsheared configurations. Rotation adds a characteristic scale to the problem, namely the radius of the light cylinder $R_{\rm LC}$. The field lines open to infinity beyond the light cylinder. We start with a non-rotating neutron star and bring it to final rotational velocity $\Omega_\star$ and then are allowed to relax to a steady equilibrium state.

We first consider the case of an aligned neutron star in purely dipolar field, and with *no* shearing of the magnetic field lines. We expect the solution to resemble that given by (Michel 1973) (equation 22), once the equilibrium has been achieved. We compared the radial momentum from simulations for a fixed θ with those generated from simulations and the values were in excellent agreement (Fig. B1). We also observe a few weak plasmoid ejection events, consistent with Parfrey et al. (2013), Fig. B2.

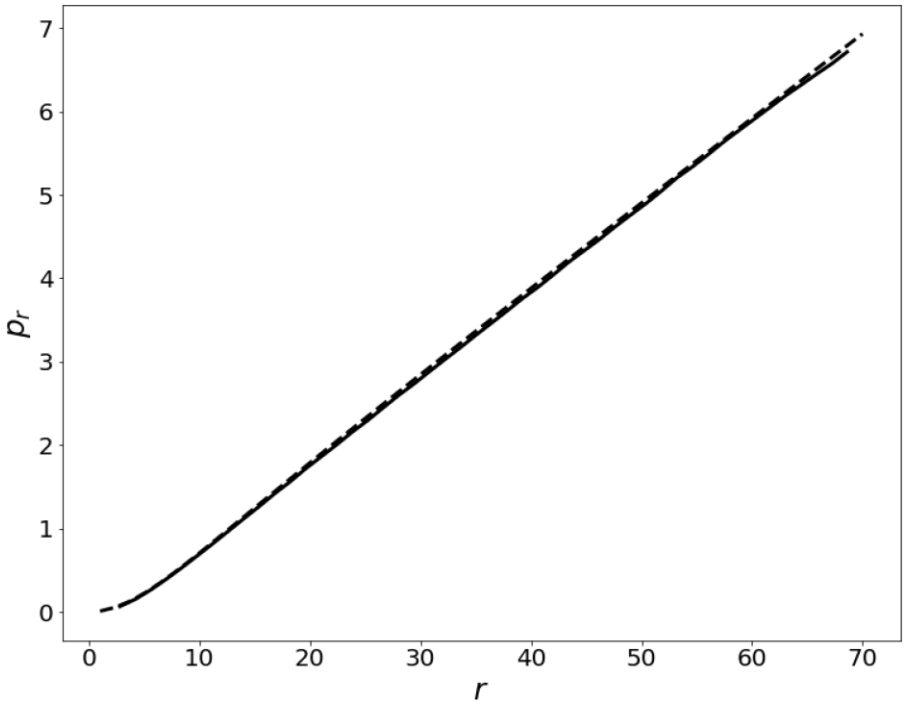

Figure B1. Radial momentum (solid) from analytical expression (equation 22) and (dashed) for a simple dipole with no flux tube from numerical simulation data at $\theta = 30^\circ$.

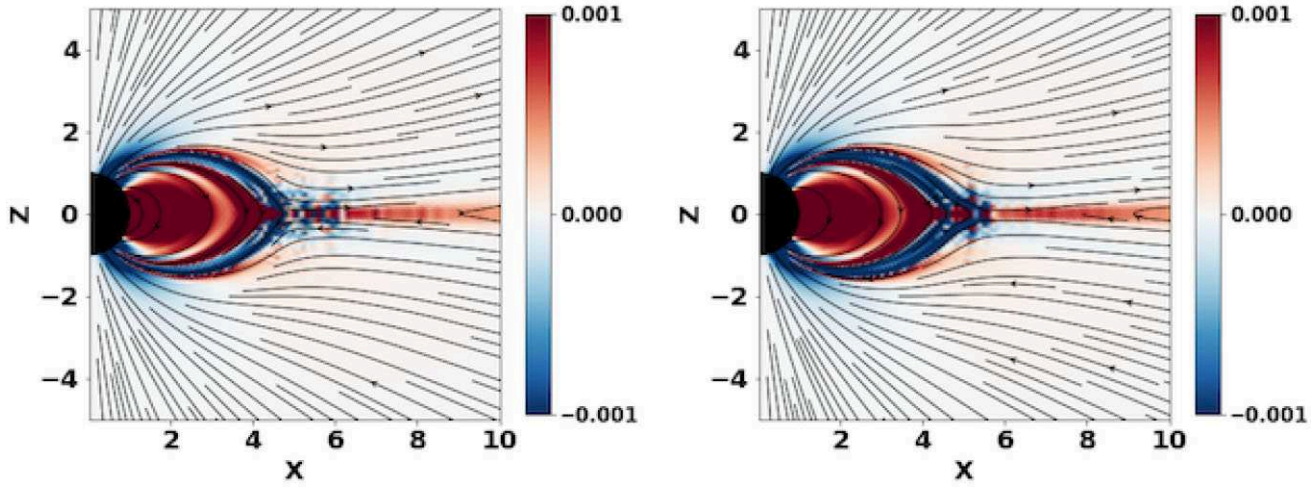

Figure B2. Toroidal current (J_ϕ) for an aligned rotating dipole ($\Omega = 0.2$) with no shearing at two consecutive time slice clearly showing plasmoid ejection.

APPENDIX C: PERTURBATIONS OF MICHEL'S SOLUTION

Using vector spherical harmonics

$$\begin{aligned} \boldsymbol{Y}_{lm} &= \boldsymbol{E}_r Y_{lm}, \\ \boldsymbol{\Psi}_{lm} &= r\nabla Y_{lm}, \\ \boldsymbol{\Phi}_{lm} &= \boldsymbol{r} \times \nabla Y_{lm}, \end{aligned} \tag{C1}$$

and Y_{lm} are scalar spherical harmonics, we look for perturbations of the vector potential with angular dependence of $\delta\mathbf{A}$ as an expansion in spherical harmonics (Abramowitz & Stegun 1972), with the following radial and temporal parametrization

$$\delta\mathbf{A} \propto f(r-t)g(r) \times \begin{cases} \mathbf{Y_{lm}} \\ \Psi_{lm} \\ \Phi_{lm} \end{cases} \tag{C2}$$

Noting that Michel's solution corresponds to

$$\begin{aligned} B_{M,r} &\propto \frac{1}{r^2}\mathbf{Y}_{00} \\ A_{M,\theta} &\propto \frac{1}{r}\Psi_{10}, \end{aligned} \tag{C3}$$

by orthogonality of vector harmonics any solution

$$\delta\mathbf{A}_1 \propto \frac{f(r-t)}{r}\Psi_{lm}$$
$$\mathrm{div}\,(\delta\mathbf{A})_1 = 0 \tag{C4}$$

satisfies the wave equation

$$\partial_t^2\delta\boldsymbol{A} - \Delta\delta\boldsymbol{A} + \nabla(\nabla\cdot\delta\boldsymbol{A}) = \boldsymbol{J} - \boldsymbol{J}_0,$$
$$\boldsymbol{J} = \frac{(\boldsymbol{B}\cdot\nabla\times\boldsymbol{B}) - (\boldsymbol{E}\cdot\nabla\times\boldsymbol{E}) + (\mathrm{div}\,\boldsymbol{E})\boldsymbol{E}\times\boldsymbol{B}}{B^2} \tag{C5}$$

and all constraints

$$\boldsymbol{B} = \boldsymbol{B}_0 + \delta\boldsymbol{B},$$
$$\boldsymbol{E} = \boldsymbol{E}_0 + \delta\boldsymbol{E},$$
$$\mathrm{div}\,\boldsymbol{B} = 0,$$
$$\boldsymbol{E}\cdot\boldsymbol{B} = 0,$$
$$\partial_t\boldsymbol{B} + \nabla\times\boldsymbol{E} = 0$$
$$\nabla\times\boldsymbol{B} = \mathbf{J} + \partial_t\boldsymbol{E} \tag{C6}$$

We also note that though generally current (C5) is a non-linear function of the fields, in this particular, case it turns out to be linear in δB.

In terms of electromagnetic fields,

$$\delta B_\theta = -im\mathrm{e}^{im\phi}P_l^m \times \frac{r_0}{r\sin\theta}\delta B(r-t) = -\delta E_\phi$$
$$\delta B_\phi = -\mathrm{e}^{im\phi}\left[(l+1)\cos\theta P_l^m + (-l+m-1)P_{l+1}^m\right] \times \frac{r_0}{r\sin\theta}\delta B(r-t) = \delta E_\theta$$
$$\delta J_r = -\frac{l(l+1)\mathrm{e}^{im\phi}(\cos\theta(l-m+1)P_{l+1}^m - \sin\theta P_{l+1}^{m+1})}{(l+m+1)} \times \frac{r_0}{r^2}\delta B(r-t) \tag{C7}$$

where $P_l^m = P_l^m(\cos\theta)$. One then recognizes (Brennan, Gralla & Jacobson 2013)

$$\delta E_\theta = \delta B_\phi = \frac{1}{r}\partial_\theta f(t-r,\theta,\phi),$$
$$\delta E_\phi = -\delta B_\theta = \frac{1}{r\sin\theta}\partial_\phi f(t-r,\theta,\phi). \tag{C8}$$

These are global, fully non-linear solutions (no limitation on δB), satisfying $E\cdot B = 0$. They cannot be separated into local X or O-mode, except $\{l, m = 0\}$ modes which are purely X-mode with electric field perpendicular to the guide field B_M. In fact, the modes have an arbitrary shape, not necessarily harmonic, so they are better referred to as pulse.

For example, for $l = 1$,

$$\boldsymbol{\Psi}_{1,-1} \propto \{0, -\cos\theta, -i\}\frac{r_0\mathrm{e}^{-i\phi}f(r-t)}{2r},$$
$$\delta\boldsymbol{B}_{1,-1} = \{0, i, \cos\theta\}\mathrm{e}^{-i\phi}\frac{r_0}{2r}\delta B(r-t),$$
$$\delta\boldsymbol{E}_{1,-1} = \{0, \cos\theta, -i\}\mathrm{e}^{-i\phi}\frac{r_0}{2r}\delta B(r-t),$$
$$\Psi_{1,0} \propto \{0, -\sin\theta, 0\}\frac{r_0}{r}f(r-t),$$
$$\delta\boldsymbol{B}_{1,0} = \{0, 0, -\sin\theta\}\frac{r_0}{r}\delta B(r-t),$$
$$\delta\boldsymbol{E}_{1,0} = \{0, -\sin\theta, 0\}\frac{r_0}{r}\delta B(r-t),$$
$$\Psi_{1,1} \propto \{0, -\cos\theta, -i\}\frac{r_0\mathrm{e}^{i\phi}f(r-t)}{r},$$
$$\delta\boldsymbol{B}_{1,1} = \{0, i, -\cos\theta\}\mathrm{e}^{i\phi}\frac{r_0}{r}\delta B(r-t),$$
$$\delta\boldsymbol{E}_{1,1} = \{0, -\cos\theta, -i\}\mathrm{e}^{i\phi}\frac{r_0}{r}\delta B(r-t). \tag{C9}$$

At a large distance, the relative amplitude $\delta B/B_\mathrm{M}$ reaches a constant.

Any $m = 0$, solution has the form $\delta B = \{0, 0, -\delta B_\phi\}$, and $\delta\mathbf{E} = \{0, -\delta B_\phi, 0\}$ – this matches Michel's solution with arbitrary $\Omega(r-t,\theta)$ Lyutikov (2011); formally, this corresponds to arbitrary sum of different l-solutions.

Another solution that satisfied the Lorentz gauge,

$$\delta\mathbf{A}_2 \propto f(r)\mathbf{Y}_{lm} + \frac{\partial_r(r^2f(r))}{l(l+1)r^2}\Psi, \tag{C10}$$

cannot be treated in this way (separation of variable).

Non-linear interaction of modes $\delta\mathrm{A}_2$ will lead to turbulent cascade and dissipation. Also, both modes $\delta\mathrm{A}_1$ and $\delta\mathrm{A}_2$ do not allow reversals of the radial magnetic field. Hence, they would interact strongly with the current sheet (e.g. Thompson 2023).

This paper has been typeset from a TEX/LATEX file prepared by the author.